A.M. High Albedo Events in Martian northern polar craters: An Investigation Using THEMIS Infrared Data

Austin Jordan and Hongjie Xie

Department of Geological Sciences, UTSA,
One UTSA Circle, San Antonio TX 78249-1644

Abstract

Following the work done on surveying High Albedo Events (HAE's) in Mars' northern polar craters (Armstrong et al., 2007), we use data from THEMIS (Thermal Emission Imaging System) on board the Mars Odyssey spacecraft to correlate the findings of the TES (Thermal Emission Spectroscopy) survey. In the TES survey, there were 9 craters (65°N to 71°N) with a diameter larger than 10km which displayed HAE's in a.m. hours (0140-0330 local time) during late spring to mid-summer, at temperatures well above the sublimation point of carbon dioxide frost. This implies that water ice forms overnight, sublimates during the day, and re-deposits in the following night (Xie et al., 2007). Using the THEMIS image database at http://themis.asu.edu, we found a total of 40 infrared images and several visible images which fell into our search criteria for the a.m. crater HAE's. These images were captured at a local time ranging from 0419-0511 during Ls 47° to 180°, with solar incidence angles ranging from 95.4° to 72.1°. An investigation of these images showed mixed results. Some craters (65.43°N/128.33°E, 66.35°N/163.44°E, 66.38°N/144.02°E, 70.04°N/352.05°E) exhibit what could be interpreted as signs of interior crater frost but none of them is definitive, while others (64.82°N/209.40°E, 64.90°N/350.77°E, 65.49°N/283.67°E, 69.87°N/285.01°E, 70.88°N/193.55°E) display no sign of interior crater frost at all. Additionally, there are a number of craters (64.90°N/350.77°E, 65.43°N/128.33°E, 66.35°N/163.44°E,

66.38°N/144.02°E, 70.04°N/352.05°E, 70.88°N/193.55°E) which show definite signs of water frost along the crater rim. These observations suggest one of the followings: (1) the interior crater frost sublimates before the THEMIS images were taken; (2) the THEMIS data cannot capture the diffuse, scattered, and thin frost deposits well enough to be used in any conclusive manner; or (3) there was simply no interior crater frost to begin with.

Introduction

It has become generally accepted in the scientific community that the Martian northern polar region contains water ice which is revealed as the CO_2 ice cap retreats in warmer seasons (Titus, T.N., 2003). It has been proposed that an ice rich regolith in the northern polar region of Mars is actively sublimating water ice in the warmer period. This water vapor then re-condenses on the surface (Bass et al., 2000). This theory has also been applied to the observations made of frost accumulation in northern polar craters (Armstrong et al., 2005).

This study was inspired by "Survey of TES high albedo events in Mars' northern polar craters" by Armstrong et al. (2007). Their research involved identifying and mapping craters in the northern polar hemisphere of Mars which displayed high albedo events. High albedo events (HAE) are the name given to the sudden increase in albedo observed during the Martian polar summer. These HAE occur after the surface temperature is well above the sublimation point of CO_2 frost (150˚K). Armstrong et al. found that that there were HAE in 18 of the 60 northern polar craters larger than 10 km. Nine of these polar craters exhibited HAE in the a.m. hours only (0140-0330 local time). It was found that the a.m. only deposits occurred in latitudes less than 70˚ and at

temperatures just below 200˚K. Armstrong et al. propose that these a.m.-only HAE's occur as a result of temporary, diurnal deposits. This implies that the source for the water ice may be from an ice-rich regolith just below the surface. In this paper we take a closer look at these 9 craters identified by Armstrong et al. to have a.m. HAE with the THEMIS instrument aboard the Mars Odyssey spacecraft.

Methods

The THEMIS instrument has a significantly higher spatial resolution than the TES instrument used in the parent study by Armstrong et al. THEMIS is equipped to capture both visual and infrared images. THEMIS has a spatial resolution of 18m/pixel for visual images and 100m/pixel for infrared images. The TES instrument used in the parent study performed by Armstrong et al. has a spatial resolution of 3000m/pixel and measures the albedo rather than the temperature.

The THEMIS image database located at Arizona State University (http://themis.asu.edu/) was used to gather images. The search criteria for each a.m. HAE crater location included constraints on both local time and solar longitude. The local time bracket was for a.m. hours only, while the solar longitude bracket was between Ls=45˚ to Ls=180˚. It is important to note that both the local time and solar longitude search brackets are expanded far beyond the limit in which the a.m. HAE would likely be found. This was done in order to assure that no HAE went unnoticed. The images which fell into these search criteria were then viewed in ENVI 4.3 to determine if any HAE could be identified at the time of image capture. Each image was manipulated in ENVI to show both relative and precise temperatures. Temperature data which may indicate frost/ice within the crater included both drastic temperature differences between the crater floor

and the surrounding plain, and distinct ground temperature variation within the crater. Once located, these ground temperature variations could often be compared to images taken on a separate date. Through contrasting images, conclusions could be made as to the nature of the temperature variations.

Results

The results of the search proved to be of varying achievement. There were a total of 40 infrared images which fit the search criteria and several visual images (Fig.1). Some of the craters were fairly underrepresented as a result of the few images captured at those locations by THEMIS.

A.M. Crater Location	Vis. Images	I.R. Images
64.82° N, 209.40°E	-	3
64.90° N, 350.77°E	4	9
65.43° N, 128.33 °E	1	6
65.49° N, 283.67°E	-	2
66.35° N, 163.44°E	-	3
66.38° N, 144.02° E	1	3
69.87° N, 285.01° E	-	1
70.04° N, 352.05° E	3	7
70.88° N, 193.55° E	-	6

Fig.1 Number and type of images captured for each crater location

No THEMIS images were available before 0419 within the search criteria. The original TES survey identified a.m. HAE in the hours from 0140-0330 local time. This inconsistency in local time with the TES observation performed by Armstrong et al. may skew much of the work. Four of the nine craters showed possible signs of frost on the crater interior (Images 1 & 2). These crater images were all captured before Ls=110˚. Five of the nine craters showed no signs of interior crater frost. With the exception of one

crater, all the images for the a.m. craters were captured at a solar longitude greater than 140˚ (Fig.2)

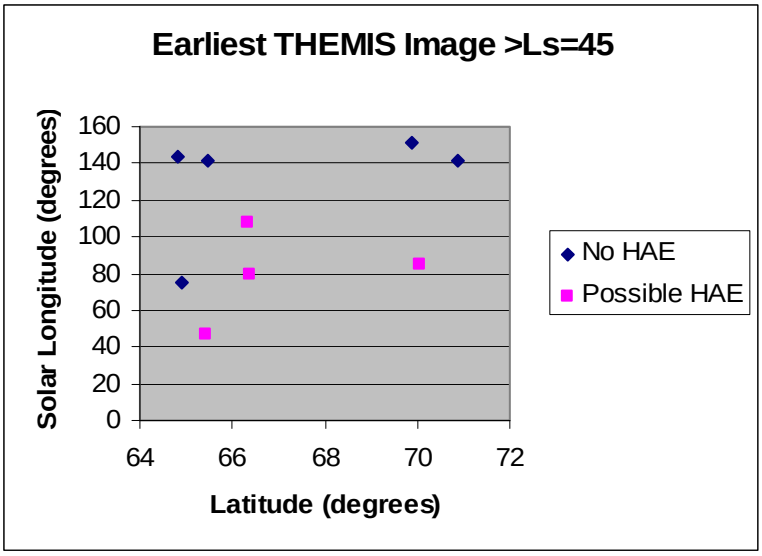

Figure 2. A correlation between craters which show no signs of HAE's and craters which may show HAE's. This graph implies that the images which show no HAE's may be the result of timing (i.e. the available images were taken too late in the Martian summer)

The diurnal HAE craters displayed a distinctly different thermal signature than those of the persistent (a.m. and p.m.) HAE craters. In the persistent HAE craters the surface temperature within the crater is consistently cooler than the surrounding plains (Armstrong, et al., 2007) (Image 3). Many of the a.m. craters showed slightly warmer interior surface temperatures (Image 4). The surface temperatures ranged from being in close equilibrium with the surrounding terrain to occasionally being of a higher temperature (10˚K+).

Six of the a.m. craters did show distinct signs of frost along the interior of the crater rim (Images 1 & 2). All of the possible a.m. HAE craters and two of the craters which showed no signs of interior frost were among this classification of frosted crater rims.

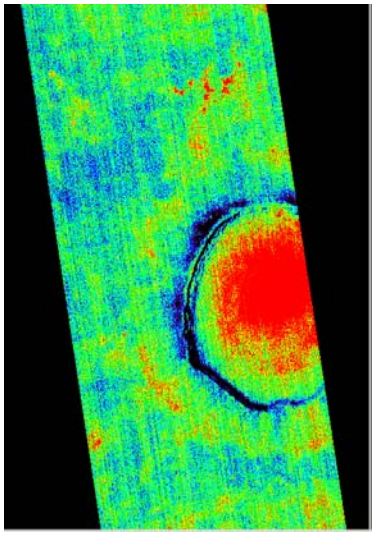

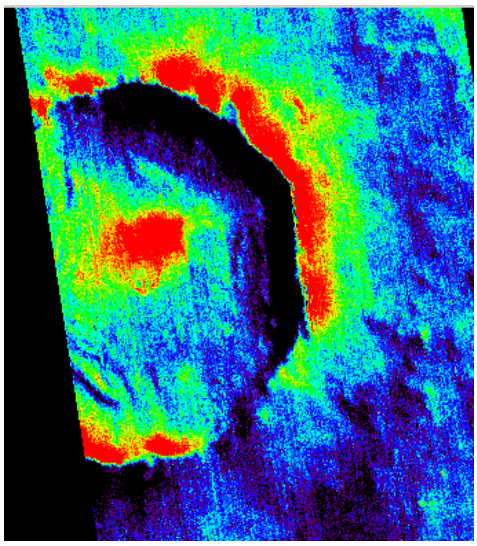

Images 1 & 2. Crater at 65.43˚N, 128.33˚E. Crater floor shows distinct temperature variations from image taken at solar longitude 47.2˚, incidence angle 81.6˚, and time 4.43 (left) to the image taken at solar longitude 69.7˚, incidence angle 75.3˚, and time 4.67 (right). Variations may be due to thin frost deposits in image on the right. There is also evidence of rim frost in both images.

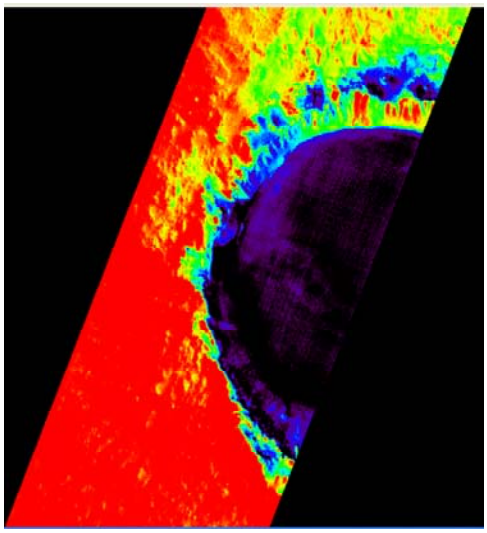

Image 3. Crater at 77.17˚N, 214.28˚E. Image taken at solar longitude 127.2˚, incidence angle 71.3˚, and time 18.4. Image of persistent (am & pm) HAE. Crater interior significantly cooler than surrounding plain.

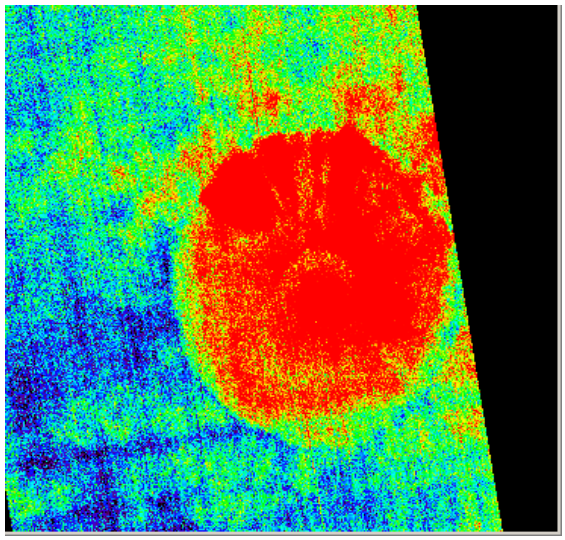

Image 4. Crater at 65.49˚N, 283.67˚E. Image taken at solar longitude 141.3˚, incidence angle 80.6˚, and time 5.09. Image shows crater interior to be warmer than surrounding plain. Crater interior of homogeneous temperature range.

Conclusions

In craters with persistent HAE's, the interior of the crater is significantly cooler than the surrounding region (Armstrong et al., 2005). This is in slight contrast with the results found in this study with the non-persistent, a.m.-only HAE craters. In many of the captured images, the interior of the crater has a higher surface temperature than the surrounding region. Differing heat capacities in the craters at: 65.43°N/128.33°E, 66.35°N/163.44°E, 66.38°N/144.02°E, and 70.04°N/352.05°E hold the possibility of a thin layer of frost having been deposited on the crater floor. However, there is no irrefutable evidence of the existence of subsurface interior crater frost in any of these images. The frost located on the crater rim is presumed to be from atmospheric capture. The atmospheric water vapor may originate from the sublimated frost within the crater or from regional atmospheric humidity. Crater rim frost persists longer than interior crater frost due to the increased protection from solar radiation. The ability of THEMIS to detect ice on several of the a.m. crater rims is evidence that the instrument is able to identify frost. The absence of any clear sign of frost on the crater floor may be simply due to the differing times (both local times and solar longitude) in which THEMIS images were available compared to the TES images used to identify HAE (Armstrong, et al., 2005, 2007). It is also possible that the frost which forms on the crater floor is too diffuse to create a significant thermal change in relation to its surroundings, unlike the frost located on some crater rims. It is also important to keep a level of skepticism and assume the possibility that there is no a.m. HAE occurring. However, with the thorough TES results from Armstrong et al., the subject certainly requires more attention. This research using the THEMIS instruments adds additional information both for and against a.m.-

only HAE. However, it is apparent that further research using more than just the THEMIS instrument will be needed in order to make any tangible conclusions about a.m.-only HAE in northern polar craters.

Acknowledgements

This work was supported by the M.O.R.E. science research program at University of Texas at San Antonio. The authors wish to acknowledge the use of THEMIS images from NASA /JPL/Arizona State University.

References

Armstrong, J., Titus, T., Kieffer, H., 2005. Evidence for subsurface water ice in Korolev crater, Mars. Icarus. 174, 360-372.

Armstrong, J., Nielson, S., Titus, T., 2007. Survey of TES high albedo events in Mars' northern polar craters. Geophysical Research Letters,34, L01202.

Bass, D. S., K. E. Herkenhoff, and D. A. Paige, (2000), Variability of Mars' north polar ice cap: I. Analysis of Mariner 9 and Viking Orbiter imaging data, *Icarus, 144,* 382-396.

Titus, T.N. (2003), CO2 cycle: two martian years of polar IR observations, *Workshop on Mars Atmosphere Modeling and Observations,* January 13-15, Granada, Spain.

Xie H., Guan H., Zhu M., Thueson M., Ackley S.F, and Zongyu Yue, (2007) A conceptual model for explanation of Albedo changes in Martian craters

Physical properties of Sea Ice from the Ross Sea, Antarctica

Undergraduate Student: Beverly Saunders
Advisor: Stephen Ackley
Department of Geological Sciences
University of Texas at San Antonio

Abstract

Thirty three ice cores were extracted at different sites along the Ross sea pack ice between the dates of Dec. 27th, 1999 and February 1st, 2000. Snow and slush depths were measured at each site and estimated ice concentrations were recorded throughout the trip. The cores were segmented into different depth intervals. Each segment was processed and observed. Ice textures were identified as granular, columnar, transitional or other, and salinity and $\delta^{18}O$ samples were taken and measured at each interval. This data was then input to a basic excel program and analyzed. The mean snow and slush depths, ice concentrations, and total percent ice type compositions were then calculated; as were the mean salinities and $\delta^{18}O$ values for each ice type for all of the cores. The ice cores were then divided into groups according to the latitude from which they were extracted and the same analyses were performed for each group. Profiles for each of the cores were also constructed. Slush was present in twenty four of the thirty two ice core locations and was common in most areas. Granular ice was the most common ice type being between 56 and 90 percent of the ice composition in each of the divided areas and over 63 percent of all of the ice sampled. The mean salinity was around 4.14‰ and the $\delta^{18}O$ mean values tended to be dominated by negative values indicating high snow ice concentrations.

Introduction

Antarctic sea ice formation and the presence of snow covered sea ice have important influences on ocean and atmospheric exchanges that affect micro and macro climates (Allison,

1982; Ackley & Lytle 2001). In light of this, it is important to understand how sea ice formation takes place in different areas in order to be able to predict how climate change will affect sea ice over and in turn the global climate. In order to gain more knowledge of both of these processes investigations of each Antarctic region have increased significantly during the end of the twentieth and the beginning of the twenty first century. As a result of these investigations, and the resulting ice formation databases, it is now accepted knowledge that high amounts of sea ice is formed over large areas through flooding and snow ice formation in addition to ice forming from seawater itself (Jeffries 2001).

Various predictions have been made as to what will occur as the climate changes. In order to observe these changes it is important to continue a time series look at the ice types in different Antarctic regions in order to confirm or deny the predictions as valid. In order to continue with this database, ice cores are taken frequently on cruises to the Antarctic to allow for accumulation of data in that area so that full pictures may be developed. While core data from one cruise cannot portray accurate ideas of spatial and temporal variability the accumulation of this data will allow for a better idea of the ice types in that occur in various regions at different times. In time this will allow for look at the changing behaviors of each regions ice formation.

The primary purpose of this paper is to look at and present analyzed data from ice cores taken in the Ross sea area between Dec. 27th 1999 and Feb. 2nd 2000. These were data sets that were never processed or looked at and need to be entered into the core data base. The secondary purpose is to compare this data to published reports on ice types and formations in the same area in order to determine a level of accuracy.

Location and Methods

Thirty three ice cores were extracted in the Ross sea area during the summer season between the latitudes and longitudes of 68 to 78 degrees south and 125 to 180 degrees west. At each core site the snow and slush depths were recorded and samples were extracted. The cores were then sectioned into varied increments dependent on the core length. At each interval the textures were identified as columnar, granular, transitional or other. Salinity and $\delta^{18}O$ measurements were then taken and recorded in parts per thousand (‰) for each snow and slush sample as well as for each interval. This data (APIS database) was then input into a basic excel program for analysis.

Each texture observation gives indication what kind of sea ice formation process took place. Columnar texture is indicative of ice that formed through one dimensional conductive heat transfer causing the formation of ice directly from sea water at the bottom of the ice flow or congelation ice. Granular can give indication of two separate formation process; the first of frazil ice formed from turbulent processes like waves in pancake ice or advection from high winds; the second of snow ice formed from the freezing of flood zones when there is a negative freeboard present (often when accumulation of snow is high). These two formations can be distinguished through $\delta^{18}O$ measurements the first having positive $\delta^{18}O$ values and the latter having negative due to the large contribution of precipitation to its formation (Jeffries and others 1997).

Based on this knowledge the $\delta^{18}O$ values and the ice texture observations were compared in order to allow for an ice type and ice formation pathway to be determined. Once these conclusions were made, salinity, $\delta^{18}O$ values and ice texture profiles for each core were produced (Appendix A) in order to allow for a visual representation of the core data and for quality assurance purposes.

Once the individual profiles were made the overall mean salinity, $\delta^{18}O$ and ice type compositions were calculated for the all the cores. The core data was then separated into groups by latitude, as shown in figure 1 below, to allow for a spatial variability analysis. The same calculations that were done for all the cores were then done for each group as well.

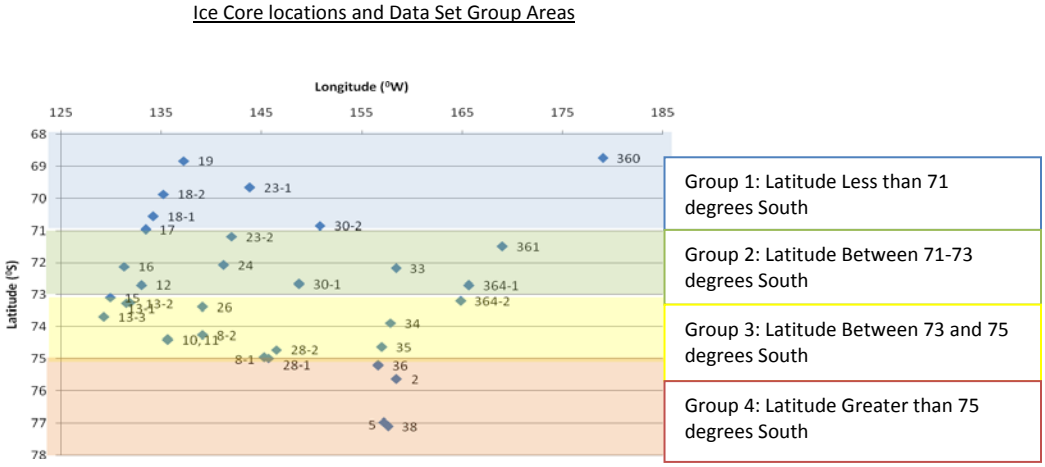

Figure 1. *Each core location graphed by latitude and longitude and identified by Julian day and core number of that day. Absence of a core number shows that only one core was taken within the given Julian day. The groups labeled represent the core spatial area in which the cores were grouped and analyzed.*

Once all of the data was calculated it was then graphed to allow for visual representation. This was done for all of the cores overall and for each group data set.

Results

The overall mean snow, slush, $\delta^{18}O$ and salinity values for all the cores, as well as the latitudinal based groups, are shown in Table 1 below. Note the largely negative $\delta^{18}O$ values and the high snow depth values.

Table 1. Mean snow and slush depths shown with the mean salinity and $\delta^{18}O$ values for 32 cores taken in the Ross Sea area during the summer season of 1999/2000. Group 1 consists of all cores at latitudes of less than 71°S; Group 2 is cores between 71°S to 73°S; Group 3 is cores between 73°S and 75°S; and Group 4 consists of all cores at latitudes greater than 75°S.

	Mean Snow Depth (cm)	Mean Slush Depth (cm)	Mean Core Salinity (‰)	Mean Core $\delta^{18}O$ (‰)
All Cores	35.4	13.8	4.14	-0.799
Group 1	31.6	17.7	3.805	-3.111
Group 2	30	21.4	4.1	-0.615
Group 3	38	12.2	4.019	0.485
Group 4	51	11	4.983	-2.431

The ice type concentration as a percentage of all the cores lengths as well as the mean salinity and $\delta^{18}O$ values for each texture are shown in figures 2A, 2B and 2C. Granular ice (both frazil and snow ice) was the most frequent ice texture.

Overall Ice Type Concentrations

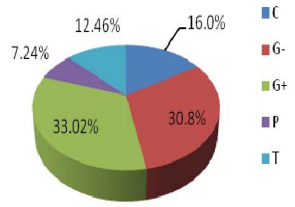

Figure 2A. *Ice type concentration as a percentage of total core length.*

Overall Ice Type Mean Salinity Values

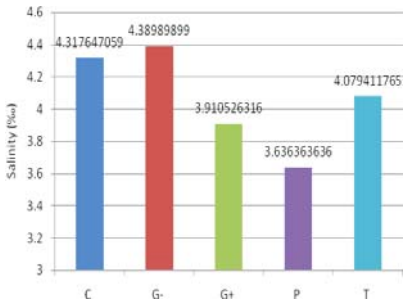

Figure 2B. *Mean salinity values of the ice types present in the Figure 2A.*

Overall Ice Type Mean $\delta^{18}O$ Values

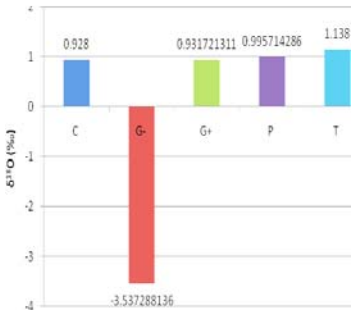

Figure 2C. *Mean $\delta^{18}O$ values of the ice type found in Figure 2A.*

Figure 2 (A, B and C) **Note**: All data extrapolated from a database of 32 ice cores extracted from Ross Sea area in summer season 1999/2000. *C = congelation ice, G- = snow ice, G+ = frazil ice, P = unidentified and T = transitional ice (2+ contributing textures).*

The ice texture percentages of the total length of the cores in Group 1 (less than 71°S) and the mean salinity and $\delta^{18}O$ values for each texture are shown in figures 3A, 3B and 3C respectively. Snow ice is the most common.

Group 1 Ice Type Concentrations

Group 1 Ice Type Mean Salinity Values

Group 1 Overall Ice Type Mean $\delta^{18}O$ Values

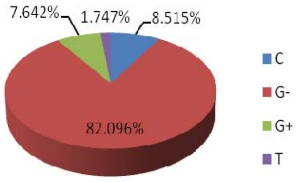

Figure 3A. *Ice type concentrations as a percentage of total core length of cores taken at latitudes less than 71°S.*

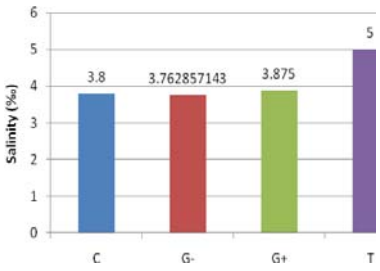

Figure 3B. *Mean salinity values of the ice types present in the Figure 3A.*

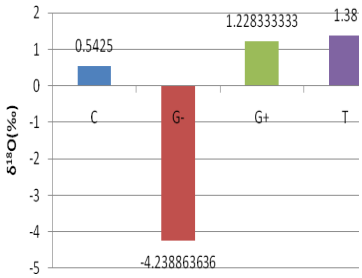

Figure 3C. *Mean $\delta^{18}O$ values of the ice type found in Figure 3A.*

Figure 3 (A, B and C) **Note**: All data extrapolated from a database of 7 ice cores extracted from Ross Sea area in summer season 1999/2000. *C = congelation ice, G- = snow ice, G+ = frazil ice, P = unidentified and T = transitional ice (2+ contributing textures).*

The ice texture percentages of the total length of the cores in Group 2 (between 71°S and 73°S) and the mean salinity and $\delta^{18}O$ values for each texture are shown in figures 4A, 4B and 4C respectively. Snow ice is still predominant but the frequency of frazil ice has increased with the rise in latitude.

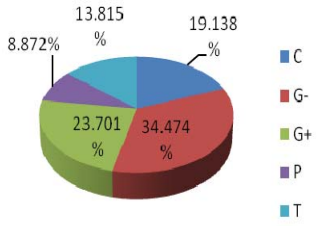

Figure 4A. *Ice type concentrations as a percentage of total core length of cores taken at latitudes between 71°S and 73°S.*

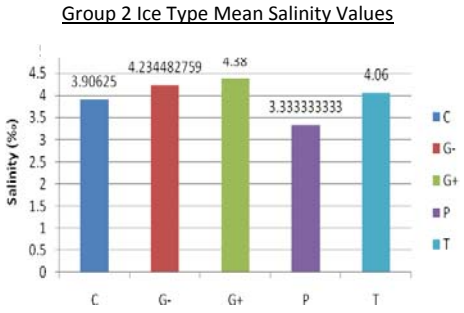

Figure 4B. *Mean salinity values of the ice types present in the Figure 4A.*

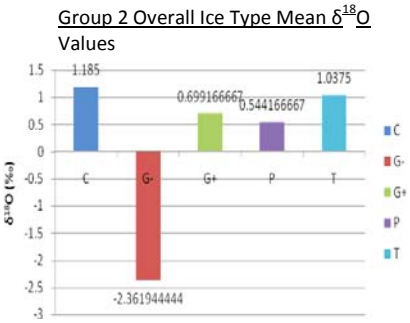

Figure 3C. *Mean $\delta^{18}O$ values of the ice type found in Figure 4A.*

Figure 4 (A, B and C) **Note**: All data extrapolated from a database of 8 ice cores extracted from Ross Sea area in summer season 1999/2000. *C = congelation ice, G- = snow ice, G+ = frazil ice, P = unidentified and T = transitional ice (2+ contributing textures).*

The ice texture percentages of the total core length of the cores in Group 3 (between 73°S and 75°S) and the mean salinity and $\delta^{18}O$ values for each texture are shown in figures 5A, 5B and 5C respectively. Frazil ice has now become dominant.

Group 3 Ice Type Concentrations (2A)

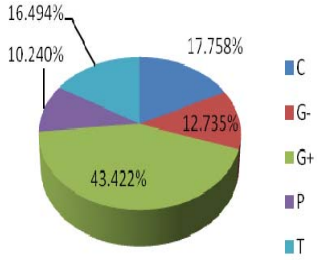

Figure 5A. *Ice type concentrations as a percentage of total core length of cores taken at latitudes between 73°S and 75°S.*

Group 3 Ice Type Mean Salinity Values

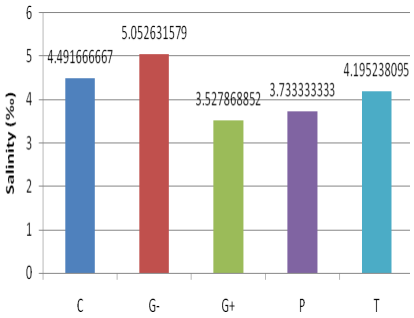

Figure 5B. *Mean salinity values of the ice types present in the Figure 5A.*

Group 3 Overall Ice Type Mean $\delta^{18}O$ Values

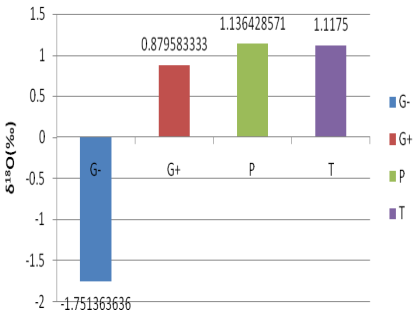

Figure 5C. *Mean $\delta^{18}O$ values of the ice type found in Figure 5A.*

Figure 5 (A, B and C) **Note**: All data extrapolated from a database of 14 ice cores extracted from Ross Sea area in summer season 1999/2000. *C = congelation ice, G- = snow ice, G+ = frazil ice, P = unidentified and T = transitional ice (2+ contributing textures).*

The ice texture percentages of the total lengths of the cores in Group 4 (greater than 75°S) and the mean salinity and $\delta^{18}O$ values for each texture are shown in figures 6A, 6B and 6C respectively. Both frazil and snow ice are quite prominent.

Group 4 Ice Type Concentrations

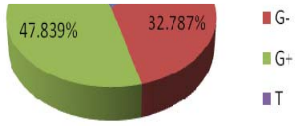

Figure 6A. *Ice type concentrations as a percentage of total core length of cores taken at latitudes above 75°S.*

Group 4 Ice Type Mean Salinity Values

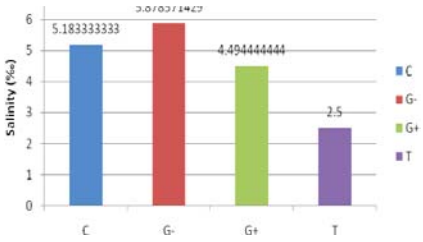

Figure 6B. *Mean salinity values of the ice types present in the Figure 5A.*

Group 4 Overall Ice Type Mean $\delta^{18}O$ Values

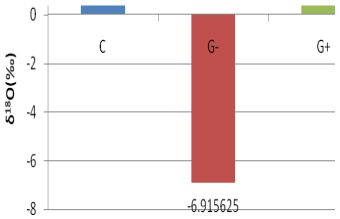

Figure 6C. *Mean $\delta^{18}O$ values of the ice type found in Figure 5A.*

Figure 6 (A, B and C) **Note**: All data extrapolated from a database of 3 ice cores extracted from Ross Sea area in summer season 1999/2000.

C = congelation ice, G- = snow ice, G+ = frazil ice, P = unidentified and T = transitional ice (2+ contributing textures).

Discussion

In the Ross, Bellingshausen and Amundsen Sea areas it has been shown that snow ice is very prevalent when looking at temporal and spatial variability (Jeffries and others 2001). This was confirmed with the data obtained from the 32 cores examined in this study. The high frequency of snow ice at ~30.8% of the total core length and over 82% of the total core length in certain data set groups (Figures 1A and 2A) gives indication of high amounts of snow accumulation in this area which is again confirmed with the mean snow depths in each group (Table 1). Accumulation of snow would be necessary in order to account for the high frequency of snow ice because large amounts of snow accumulation would be needed to overcome ice buoyancy; cause flooding and in turn cause the snow ice formation.

The individual core salinity profiles (Appendix A) show indication of higher salinities in the upper and lower regions of the ice cores. This could largely account for the higher salinity measurements in both congelation and snow ice which was present in almost all of the groups examined (Fig. 2B, 3B, 5B and 6B). This salinity gradient would likely be due to the fact that both ice types tend to form at the bottom and top of the core respectively where either slush or sea water is present.

Summary and Conclusion

The information obtained from this study was consistent with previous studies in the same general area. The high occurrence of snow ice confirms the presence a large volumes of snow accumulation and the core salinity and $\delta^{18}O$ profiles are intuitively accurate.

While all of the information obtained from this study does not have completely relevant information due to the small size of the data sets; the information is very important when put in a large data base. It is important to keep in mind that while this information is needed to allow for addition and validation of current information; more cores need to be accumulated in the area over a longer piece of time to allow for a larger picture.

Future research should consist of gathering ice core data from the Ross Sea area from other cruises to allow for a larger database. This will allow for better statistical analyses and for a more accurate picture. Using these larger data bases over a time series will also allow for confirmation or denial of predictions of how climate change affects the Antarctic precipitation and in turn the prominent sea ice types.

NOTE: Appendix A not attached due to large number of data and diagrams and will be available upon request.

Acknowledgements

I first want to thank my advisor Steven Ackley for giving me such great opportunities over the past year. I learned a great deal about lab work and data analysis as well as experimental designs and project plans that I feel far more prepared to begin my graduate studies.

I would also like to thank the MORE science program for the funding given to me to allow for me to proceed with this project and various others. The opportunities this funding has provided for me has allowed me to truly get a true look into life as a researcher.

Bibliography

I. Allison. 1982. The role of sea ice in climate variations. *In report of the WM/CAS-JSC-CCCO meeting of experts on the role of Sea ice in Climate variations, Geneva, 24-29 June 1982.* Geneva, World Meteorological Organization, 27-50.

Martin O. Jeffries, H. Roy Krouse, Barbara Hurst-Cushing, Ted Maksym. 2001. Snow ice accretion and snow-cover depletion of Antarctic first-year sea-ice floes. *Annals of Glaciology Vol. 33*. International Glaciology Society. 51-59.

Martin O. Jeffries, A.P. Worby, K. Morris, W.F. Weeks. 1997. Seasonal variations in properties and structural composition of sea ice and snow cover in the Bellingshausen and Amundsen Sea, Antarctica. *J. Glaciol.,*138-151.

V.I. Lytle, S.F. Ackley. 2001. Snow-ice growth: a freshwater flux inhibiting deep convection in the Weddell Sea, Antarctica. *Annals of Glaciology Vol. 33.* International Glaciology Society. 45-50.

Stable Carbon and Oxygen Isotopic Composition of soil and Snail shells Recovered from Archaeological Site 41KM69, Flatrock Road Site, Texas: Inferences on Ecological Conditions

Undergraduate Student
Kristi Salazar

Advisor
Dr. Debajyoti Paul
Department of Geological Sciences
University of Texas at San Antonio

Abstract

This study focuses on utilizing the stable carbon and oxygen isotopic composition of soil inorganic carbonate, soil organic matter (SOM), and shell carbonates recovered from the Archaeological site in Texas, to interpret ecological conditions prevailing during soil formation (2340-2120 B.P). Our results suggest dietary effects (C3 vs. C4) on the carbon isotopic composition of snail shells. Furthermore, carbon isotopic composition of shell carbonate is influenced by the isotopic composition of soil carbonate. Isotopic compositions of archaeological shells are consistent with that observed for the modern shells collected from the study area. Although the interpretation of oxygen isotope composition in land snails is not straightforward, values are probably related to several different climate signals including temperature, rainfall, and relative humidity, and may be used for potential markers of local climate conditions (Balakrishnan, 2004).

Introduction

We currently have a general understanding of climate and vegetation changes in the southern Great Plains of the United States during the Holocene. Climate proxy data commonly used to reconstruct aspects of climate and ecological conditions include analysis of arboreal and grass pollen frequencies from rock shelters and bogs (e.g., Bousman, 1998; Nickels and Mauldin, 2001), shifts in frequencies and presence/ absence of fossil vertebrates (e.g., Toomey, 1993) and invertebrates (e.g., Elias, 2001), changes in geomorphic patterns associated with shifts in runoff and stream flow (e.g., Nordt, 2004), and changes in stable isotope ratios in paleosols (e.g., Boutton et al., 1998; Nordt, 2002) or carbonates (e.g., Humphrey and Ferring, 2001). In this regard, stable carbon and oxygen isotopic composition ($\delta^{13}C$ and $\delta^{18}O$) of archaeological soils

and fossil assemblages (e.g., small herbivores and snail shells) can be used as proxy and document climate variability and vegetation patterns at short temporal and small spatial scales (e.g., Humphrey and Ferring, 1992; Metref et al., 2003; Balakrishnan et al., 2005), for it is at this scale that human adaptation is likely to be initiated.

The use of land snails is common in paleoenvironmental studies (e.g., Goodfriend and Ellis, 2002; Balakrishnan et al., 2005). Land snails have relatively short life spans (< 10 years) and commonly occupy lifetime ranges on the order of a few hectares, which make them potentially ideal markers of local climate conditions. Many of the uses of land snails in paleoclimate research have focused on variations in $\delta^{18}O$ in shell carbonate as indicators of shifts in the isotopic composition of rainfall (Yates et al., 2002). However, the interpretation of oxygen isotopic signatures in land snails is not straight-forward. Recent work (e.g., Balakrishnan and Yapp, 2004; Balakrishnan et al., 2005) further documents that $\delta^{18}O$ of land snail shell is probably related to several different climate signals including temperature, rainfall, and relative humidity. Furthermore, plants that use a C3 or C4 photosynthetic pathway produce distinct $\delta^{13}C$ signature; average $\delta^{13}C$ of C3 plants is ~ -27‰ while that of C4 plants is ~ -13‰. Soil Organic Matter (SOM) is comprised mainly of the decomposed plant tissue of the vegetation communities that grow on the soil cover. Therefore, $\delta^{13}C$ composition of SOM and snail shells can be used a proxy to determine snail diet and vegetation patterns. Using multiple samples from several different land snail species from the Southern Great Plains, Balakrishnan et al. (2005) conclude that while there is considerable variability in $\delta^{13}C$ values in a given setting, in general, snail shells collected from settings where C4 vegetation was dominate averaged -2.8‰ (range from -4.3‰ to -1.9‰), whereas those collected in C3 vegetation regimes averaged -9.0‰, with a range of -10.0‰ to -8.8‰.

The primary objective of this research is to utilize the $\delta^{13}C$ and $\delta^{18}O$ isotopic composition of soil and snail shells recovered from an Archaeological site 41KM69 located in Junction, Kimble County, Texas, to reconstruct ecological conditions during soil formation. A secondary objective is to test whether or not $\delta^{18}O$ of gastropod shells can be used as a reliable climate proxy.

Sampling Location and Sample Types

Using several excavation methods, the Center for Archaeological Research (CAR) recovered lithic tools, debitage, native ceramics, animal bone, snail and mussel shell, charred plant remains, and soil samples from site 41KM69 (Figure 1). About 130cm thick soil profile was excavated, with samples taken at 5cm intervals. The entire unit has been radiocarbon dated to 2340-2120 B.P. Unfortunately, the section between 10 cm to 60 cm was either missing or not properly preserved for isotopic studies, and therefore, excluded from this study. We recovered several species of terrestrial gastropod shells (Polygyra, Rabdotus, Helisoma, and Helicina Species) within the soil samples at various depths (Figure 2). Terrestrial gastropods have a short life span, so adult snails show a longer range of ecological conditions. Therefore, during hand picking shells, preference was given to choose adult samples over juvenile ones, and also to collect whole shells. We have also collected modern snail shells from the study area for comparison with the archaeological shells.

Analytical Technique

Carbon and oxygen isotopic composition of soil- and shell-carbonate were obtained in continuous flow Isotope Ratio Mass Spectrometry (CF-IRMS) by analyzing the sample CO_2 gas released by carbonate-orthophosphoric acid reaction at 72 ^{o}C (1 hr) in Gasbench II . Shell carbonate samples were rinsed in deionized (DI) water, and then placed in an ultrasonic bath for 30 minutes in order to remove adhering materials. Prior to sample-acid reaction and subsequent isotopic analyses of soil- and shell-carbonates, samples were treated with 5% sodium hypochlorite to remove the organic carbon content, dried, and powdered. Prior to isotopic analysis of SOM, soil was washed with DI water, dried, and powdered. Then powdered samples were treated with 4% HCl to remove the inorganic soil carbonate fraction. $\delta^{13}C$ of SOM was obtained by combusting the samples in a CHNS Elemental Analyzer to produce CO_2, and subsequently analyzing the isotopic composition of CO_2 in the stable isotope mass spectrometer. All isotopic composition is reported in the standard δ notation. The raw sample δ values (relative to the reference CO_2 tank value) are normalized against the international carbonate external standards, and reported in the VPDB (Vienna Pee Dee Belemnite) carbon isotope reference scale by using a multi-point linear calibration as suggested by Paul et al. (2007).

Results and Discussion

All stable carbon ($\delta^{13}C$) and oxygen ($\delta^{18}O$) isotopic data obtained in this study are presented in Table 1. Isotopic composition of soil carbonates are shown in Figure 3. $\delta^{13}C$ of carbonates in the soil profile varies in the range -2.15 to -4.63‰, where as $\delta^{18}O$ of carbonates show little variation within the profile, ranging from -3.22 to -3.92‰. Large variation in $\delta^{13}C$ values, in particular, at depths 60-80 cm, may be related to variation in ecological parameters and the source of carbon in the study area. Since oxygen isotopic fractionation between carbonate and water is a function of temperature, a restricted range in $\delta^{18}O$ of carbonates may suggest a narrow range in temperatures at which carbonate precipitation occurred.

$\delta^{13}C$ of SOM shows strong linear correlation with depth (Figure 4). It varies from -25.61‰ on the top to -22.83‰ at the bottom of the profile. The isotopic composition suggests that C3 plants were predominant in the study area. However, the higher $\delta^{13}C$ values towards the bottom of the profile may have resulted due to contribution from C4 plants (average $\delta^{13}C$ of -13 ‰). The overall ~3‰ enrichment in the heavier ^{13}C isotope at the bottom of profile relative to the organic matter present at the top, may also have resulted due to microbial metabolism during decay of organic matter. However, the observed strong linear correlation between $\delta^{13}C$ vs. depth argues against microbial decay. Previous studies have shown that $\delta^{13}C$ of modern soil carbonates are higher by 14-16‰ than SOM, whereas our results show about 20‰ difference.

$\delta^{13}C$ of shell carbonates that includes species Rabdotus, Polygyra, Helicina, Helisoma, vary in the range -5.34 to -9.53‰ and are similar to the range obtained for modern snail shells (Figure 5). A strong linear correlation ($R^2 = 0.89$) is observed for data restricted to 67.5 cm to 112.5 cm depth, which may be due to diagenesis, resulting in preferential loss of ^{12}C isotope, thus producing higher $\delta^{13}C$ values at depth. Isotopic results also suggest that using snail shell parts rather than whole shells give unreliable results. Shell growth is reliant upon many conditions (such as periods of snail activity during warmer and wetter seasons, climate, temperature, and diet etc.), so different shell parts may differ in isotopic composition. Therefore, isotopic composition of whole shell should be used as a climate proxy. Metref et al. (2003) studied the dietary effects on the $\delta^{13}C$ composition of one specific snail species *Helix aspersa Maxima* and concluded that $\delta^{13}C$ values in snail shell document snail diet. Balakrishnan et al. (2005) have shown that $\delta^{13}C$ of shells in C3 vegetation regimes range from -10.0‰ to -8.8‰,

which is consistent with our results, though our results show comparatively higher $\delta^{13}C$ values. In contrast, snail shells collected from C4 vegetation dominated areas, averaged -2.8‰ displaying a range from -4.3‰ to -1.9‰ (Balakrishnan et al., 2005). Our data shows that $\delta^{13}C$ compositions of shells are close to the average $\delta^{13}C$ of C4 plants. It is not clear whether the observed $\delta^{13}C$ of shells in C3 dominated areas are a result of C3 diet (in which case, carbon isotope fractionation results in about 15‰ higher values in the shell than the diet) or simply selective C4 diet even though C3 vegetation is predominant. Furthermore, modern day plants in the study area are predominantly C3, with the exception of C4 grasses and prickly pear (CAM plant). C4 grasses thrive during wetter seasons, and therefore, are more prominent during the summer months in the study area. This coincides with the growth periods of snails, which tend to form shells during these periods. Therefore, it is possible that snails selectively prefer C4 or CAM vegetation as diet. Furthermore, Goodfriend and Ellis (2002) demonstrate a significant relationship between vegetation cover and $\delta^{13}C$ values in shell, with heavier vegetation cover yielding isotopic values in shell that are depleted in ^{13}C (lower $\delta^{13}C$ values), and isotopic values in shell being enriched in ^{13}C (higher $\delta^{13}C$ values) in areas of lower vegetation density. It is possible that some of the variations observed in Figure 5 are related to the density of vegetation cover.

$\delta^{18}O$ of shell carbonates range from -4.77‰ to -0.71‰ and show no systematic correlation with depth (Figure 6). It is evident from the figure that Helisoma species are depleted in ^{18}O isotope (resulting in lower $\delta^{18}O$) compared to the remaining species. This may be attributed to species dependent oxygen isotope fractionation effect. It is interesting to note that Helisoma sp. also show a distinct isotopic signature in the $\delta^{13}C$- $\delta^{18}O$ space (Figure 7), which may serve as an indicator for ecological conditions in which these snails thrive. However, the oxygen isotopic signature in land snails is a function of several different climate signals including temperature, rainfall, and relative humidity, therefore, the climate interpretations are not straightforward. Furthermore, as shell growth only occurs when snails are active, and as many land snails are active under restricted temperature and moisture constraints (Thompson and Cheny, 1996), climate variability as expressed in $\delta^{18}O$ in land snail shell may be narrowly restricted relative to actual climate variation.

Figure 8 reveals good linear correlation between $\delta^{13}C$ of shell carbonates and soil carbonates ($R^2 = 0.75$, excluding the data for Helisoma). This supports the findings of Magaritz et al. (1981) that soil carbonate is also a potential source of carbon in the shell carbonate.

Conclusions

Results obtained in this study suggests that stable isotopic composition of archaeological materials such as soils and land snails can be used as a proxy to reconstruct several climate and ecological parameters such as temperature, vegetation pattern, snail diet etc. $\delta^{13}C$ compositions of SOM from archaeological soil indicate a transition from C4 to C3 dominated vegetation with time, which corresponds with other studies in the Texas regions (Boutton et al., 1998). Although vegetation patterns may have shifted, $\delta^{18}O$ of soil carbonates suggests little variation in temperature in the study area around 2200 Yr BP. $\delta^{13}C$ composition of snail shells reflect the snail diet, and when used in conjunction with the $\delta^{18}O$ compositions may serve as an indicator for specific ecological conditions under which certain snail species thrive. Furthermore, carbon isotopic composition of shell carbonate is influenced by the isotopic composition of soil carbonate. Isotopic compositions of archaeological shells are consistent with that observed for the modern shells collected from the study area, albeit minor differences. Developing an understanding of variability in stable isotopic composition in terrestrial snails, as well as understanding the implications of that variability for reconstruction of both vegetation and climate, will have relevance in a variety of archaeological settings, leading to reconstruction of climate variability at short temporal scales and at small spatial scales during the Holocene.

Acknowledgements

The author would like to thank Dr. Debajyoti Paul for his time and dedication, the MORE Science project for making our research possible, Dr. Raymond Mauldin for shell identification, and Dr. Janis Bush for plant identification (on-going).

References

Balakrishnan, M., and Yapp, C. (2004). Flux balance models for the oxygen and carbon isotope compositions of land snail shells. *Geochimica et Cosmochimica Acta* 68:2007-2024.

Balakrishnan, M., Yapp, C., Theler, J., Carter, B., and Wyckoff, D. (2005). Environmental significance of $^{13}C/^{12}C$ and $^{18}O/^{16}O$ ratios of modern land-snail shells from the southern great plains of North America. *Quaternary Research* 63: 15-30.

Bousman, C. B. (1998). Paleoenvironmental Change in Central Texas: The Palynological Evidence. *Plains Anthropologist* 43(164): 201-219

Boutton, T., Archer, S., Midwood, A., Zitzer, S., and Bol, R. (1997). $\delta^{13}C$ values of soil organic carbon and their use in documenting vegetation change in a subtropical savanna ecosystem. *Geoderma* 82: 5-41.

Boutton, T.W., S.A. Archer, A.J. Midwood, S.F. Zitzer, and R. Bol. (1998). $\delta^{13}C$ values of soil organic carbon and their use in documenting vegetation changes in a subtropical savanna ecosystem. *Geoderma* 82:5-41.

Elias, S. A. (2001). Paleoenvironmental Significance of Late Glacial Insect Fossil Assemblages from the Aubrey Site, North Central Texas. In *The Archaeology and Paleoecology of the Aubrey Clovis Site (41DN479) Denton County, Texas*. Center for Environmental Archaeology, Department of Geography, University of North Texas, Denton.

Goodfriend, G. and G. L. Ellis. (2002). Stable carbon and oxygen variations in modern *Rabdotus* land snail shells in the southern Great Plains, USA, and their relation to environment. *Geochemica et Cosmochemica Acta*. 66: 1987-2002.

Humprey, J. and C. R. Ferring. (2001). Stable Isotopic Evidence from Late Pleistocene to Holocene Climatic Change, North-Central Texas. *Quaternary Research* 41:200-213.

Magaritz, M., Kaufman, A., Yaalon, D. (1981). Calcium carbonate nodules in soils: $^{13}O/^{16}O$ and $^{13}C/^{12}C$ ratios and ^{14}C contents. *Geoderma* 25: 157-172.

Metref, S., Rousseau, D., Bentaleb, I., Labonne, M., and Vianey-Liaud, M. (2003). Study of the diet effect on $\delta^{13}C$ of shell carbonate of the land snail Helix aspersa in experimental conditions. *Earth and Planetary Science Letters* 211: 381-393.

Nickels, D. and Mauldin, R. (2001). *The Project Environment.* In *An Archaeological Survey of Twin Buttes Reservoir, Tom Green County, Texas*, edited by Raymond Mauldin and David L. Nickels, pp. 25-38. Archaeological Survey Report, No. 300, Center for Archaeological Research, The University of Texas at San Antonio.

Nordt. (2002). C_4 Plant Productivity and Climate-CO_2 Variations in South-Central Texas during the Late Quaternary. *Quaternary Research* 58(2):182-188.

Nordt. (2004). Late Quaternary alluvial stratigraphy of a low-order tributary in central texas, SA and its response to climate and sediment supply. *Quaternary Research* 62:289-300.

Paul, D., Skrzypek, G., and Istvan, F. (2007). Normalization of measured stable isotopic compositions to isotope reference scales - a review, Rapid Commun. Mass Spectrom., 21, 3006–3014, DOI: 10.1002/rcm.3185.

Thompson, R., and Cheny, S. (1996). *Raising Snails*. National Agriculture Library Special reference briefs. NAL 96-05.

Toomey, R. S. (1993). Late Pleistocene and Holocene Fauna Changes at Hall's Cave, Kerr County, Texas. Unpublished Ph.D. dissertation, The University of Texas at Austin.

Yates, T. J. S., B. F. Spiro and C. Vita-Finzi. (2002). Stable isotope variability and the selection of mollusk shell samples for ^{14}C dating. *Quaternary International* 87:87-100.

Table 1. Stable isotopic composition ($\delta^{13}C$ and $\delta^{18}O$ in VPDB scale) of soil carbonate, Soil Organic Matter (SOM), and snail shell carbonates recovered from the archaeological site 41KM69 located in Junction, Kimble County, Texas.

Depth (cm)	$\delta^{13}C$ Soil Carbonate	$\delta^{13}C$ SOM	$\delta^{18}O$ Soil $CaCO_3$	Shell Species	$\delta^{13}C$ Shell	$\delta^{18}O$ Shell
3.5	-4.46	-25.61	-3.55	Helicina	-7.47	-1.53
3.5	-4.46	-25.61	-3.55	Helicina	-7.32	-1.83
7.5	-4.63	-24.70	-3.89	Rabdotus	-8.99	-0.99
7.5	-4.63	-24.70	-3.89	Polygyra	-8.53	-1.86
7.5	-4.63	-24.70	-3.89	Helicina	-8.60	-0.77
7.5	-4.63	-24.70	-3.89	Helicina	-8.51	-0.85
7.5	-4.63	-24.70	-3.89	Helicina	-6.53	-0.71
62.5	-2.15	-23.57	-3.74	No shell present		
67.5	-2.91	-23.08	-3.44	Helisoma	-9.53	-4.34
72.5	-3.09	-23.68	-3.92	Unknown	-6.24	-1.50
72.5	-3.09	-23.68	-3.92	Helisoma	-9.16	-4.58
77.5	-4.24	-23.47	-3.52	Helisoma	-8.65	-4.77
82.5	-3.56	-23.24	-3.66	No shell present		
87.5	-3.84	-23.82	-3.65	No shell present		
92.5	-4.13	-23.40	-3.53	Polygyra	-6.89	-1.58
92.5	-4.13	-23.40	-3.53	Polygyra	-6.85	-1.65
92.5	-4.13	-23.40	-3.53	Helicina	-7.84	-2.21
97.5	-4.05	-23.24	-3.79	No shell present		
102.5	-3.92	-23.13	-3.52	Helicina	-7.56	-0.72
102.5	-3.92	-23.13	-3.52	Helicina	-6.05	-1.07
102.5	-3.92	-23.13	-3.52	Helicina	-6.03	-0.98
107.5	-3.86	-22.95	-3.73	No shell present		
112.5	-2.78	-22.83	-3.22	Helicina	-5.47	-1.78
112.5	-2.78	-22.83	-3.22	Helicina	-5.34	-1.79

Note: $\delta^{13}C$ of modern snail shells analyzed in this study gives a range from -5.49 to -8.97‰, whereas the $\delta^{18}O$ of shells range from 0.54 to -2.88‰.

Figure 1. Excavation at the Archaeological site 41KM69 located in Junction, Kimble County, Texas.

Polygyra

Rabdotus

Helisoma

Helicima

Figure 2. Four different species of land snail shells (both whole-carbonate shells and fragments) recovered from the archaeological soils at different depths from the sampling site in Figure 1.

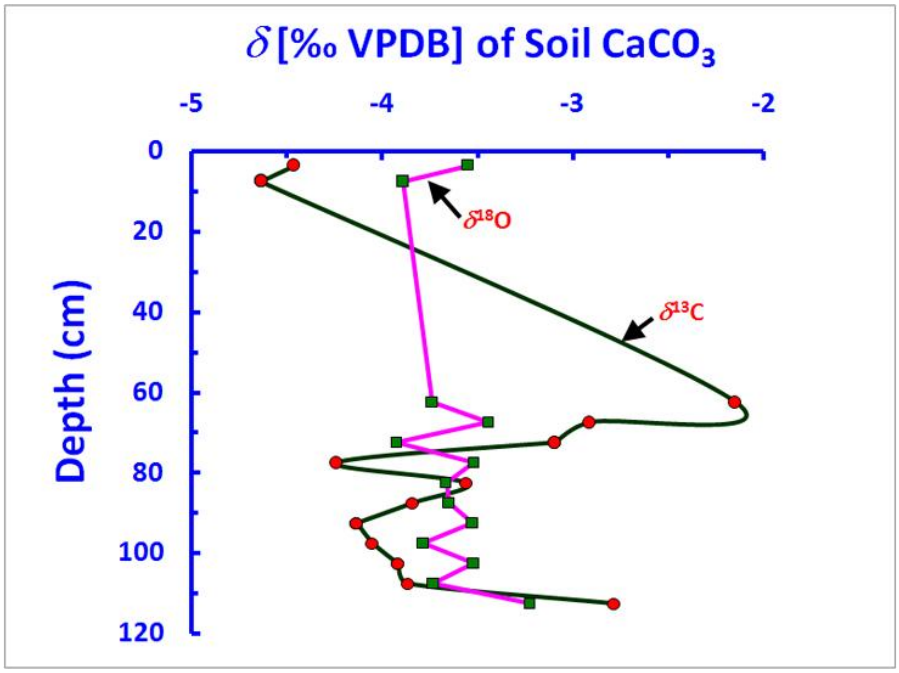

Figure 3. Variation in $\delta^{13}C$ and $\delta^{18}O$ of soil carbonate in the soil profile

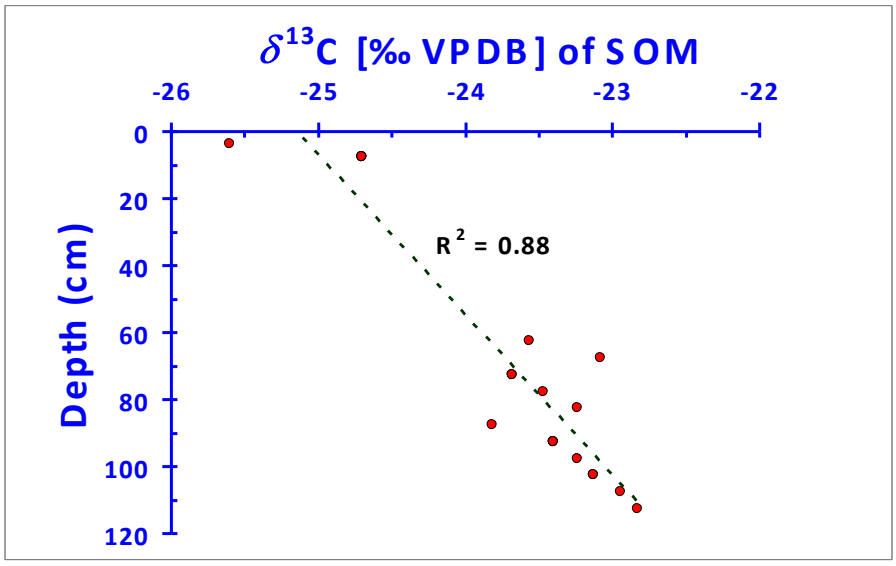

Figure 4. $\delta^{13}C$ of soil organic matter as a function of depth, where a strong linear correlation is observed. Isotopic compositions suggests C3 plants were predominate in the area.

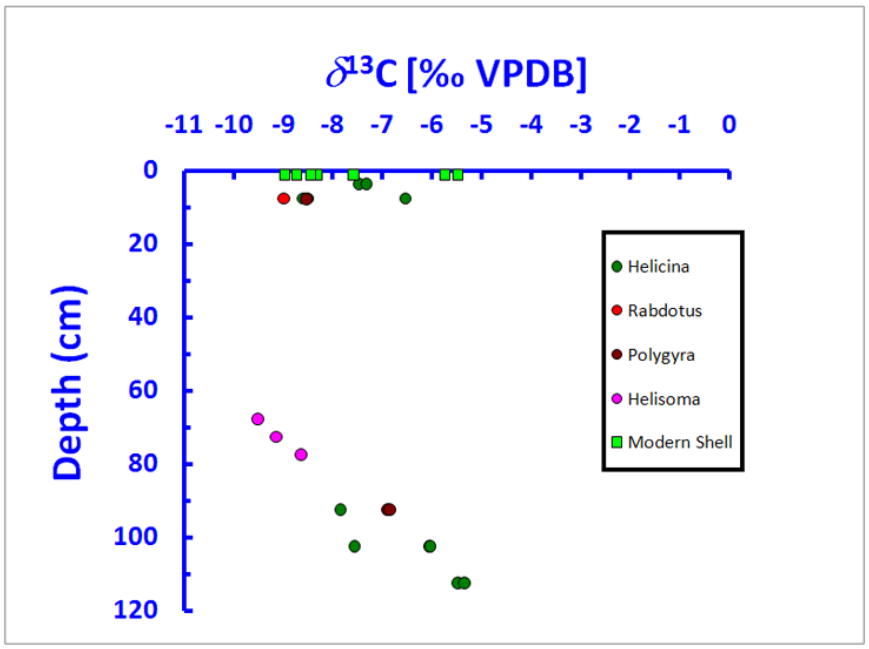

Figure 5. $\delta^{13}C$ of shell carbonates from four gastropod species (Rabdotus, Polygyra, Helicina, Helisoma) recovered from the soil. Also shown for comparison are data for modern snail shells obtained in this study.

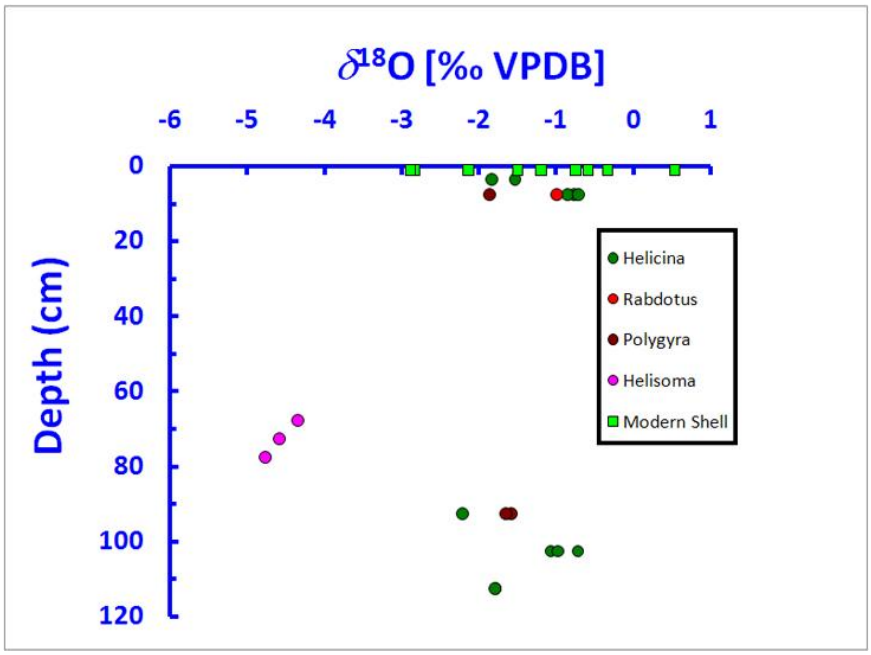

Figure 6. Variation in $\delta^{18}O$ of shell carbonates with depth. Isotopic compositions of modern shells are also shown for comparison. Distinct isotopic composition of Helisoma compared with that of other species suggest species dependent oxygen isotopic fractionation.

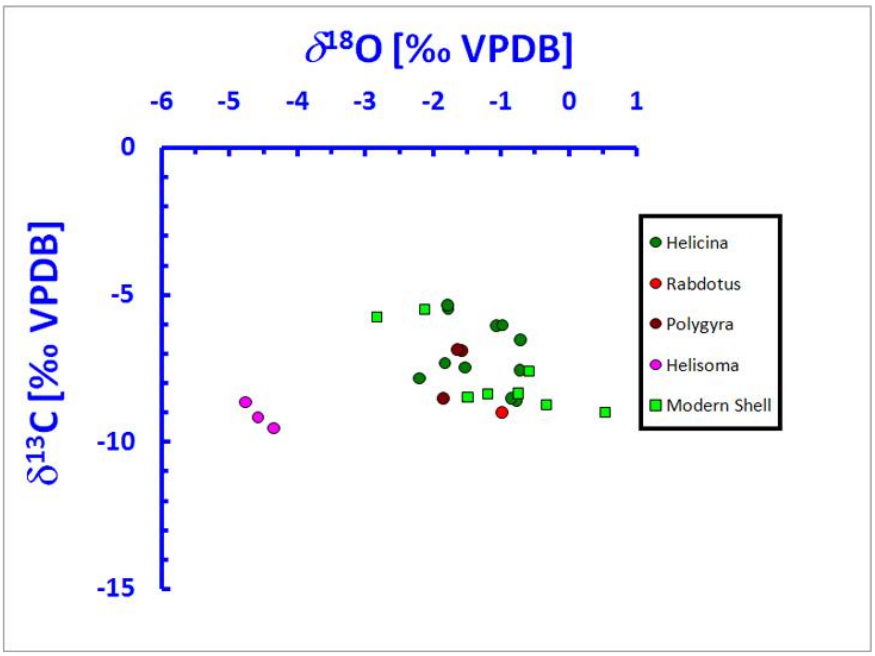

Figure 7. $\delta^{13}C$ and $\delta^{18}O$ composition of archaeological and modern shell carbonates. Note the distinct field of Helisoma species.

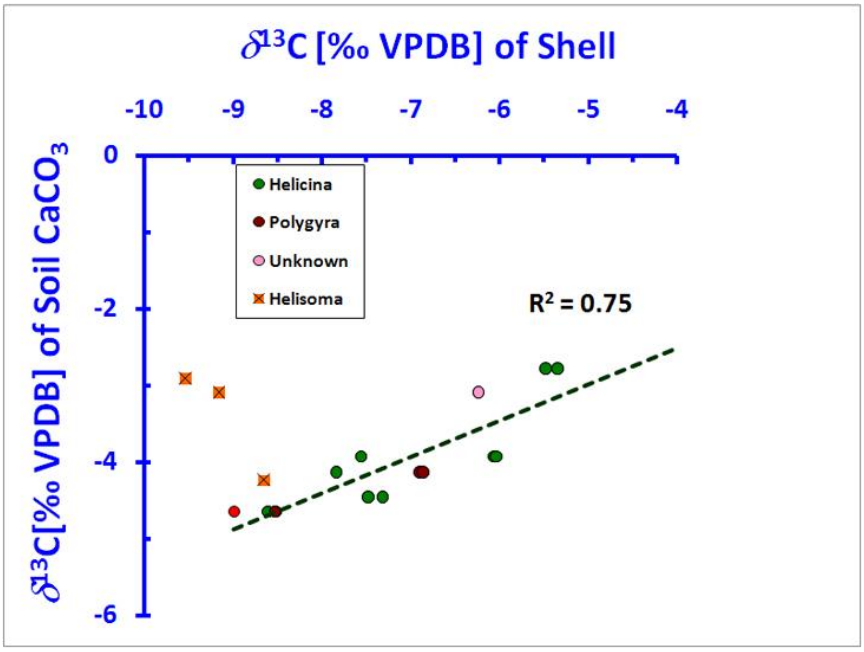

Figure 8. Relationship between $\delta^{13}C$ of shell carbonate and soil carbonate. Results for Helisoma are excluded from the correlation.

Understanding the History, Features, Modeling, and Concerns Edwards Aquifer: San Antonio Region

by
Mark Childre and Alan Dutton

Minority Opportunities Research Experience
Science Program

8 February 2008

Sponsored by: Alan R. Dutton
Department of Geological Sciences

Abstract:

Various maps of the Edwards Aquifer conduit segments, sub-regional flow direction, and potentiometric contours were made using finite difference, GIS, and mapping software. The approach took into account the hypothesis of the discontinuities created by barrier faulting and suspected cross-flow conduits. Recent research has provided evidence for the next modeling effort.

The normal faulting occurred during the late Oligocene and early Miocene Epoch which formed the Balcones Fault Zone. The geologic structure compounds the recharge and artesian characteristics of the aquifer extensively. There are problems with the possible hydraulic connection across fault zones. The original hypothesis stated a partial loss of the hydraulic connection in the recharge zone was the effect of confined or ramp faults and en echelon fractures. Edwards Aquifer Authority recently conducted tracer tests which show that the previous hypothesis is inadequate to explain the flow of water. A conduit, or a trough, may be parallel or provide perpendicular flow. These karst features may penetrate the throw of barrier faults and confined bedding that occupies a region between the Trinity and Edwards Aquifer. In the future, research is needed to further define the locations and influence of penetrating conduits and barrier faults.

Generally, the artesian zone flows freely. In the artesian zone, water moves under low hydraulic gradients through fractured karstic strata from the western counties, through the San Antonio area, northeast to Austin.

The responsibility for research of barrier faults and conduits is currently underway. By working in concert, providing definition, testing, and modeling of barrier faults, conduits, and caves of the Edwards Aquifer are being tackled. San Antonio will be ensured of an uninterruptable contamination free water supply. The research will, with continued support, promise San Antonio's rapid growth in the future.

1. Introduction:

The Edwards Aquifer of south-central Texas is noted as one of the most permeable, prolific, productive, high-volume, high flow rate aquifers in the United States. Many wells produce in excess of 20,000 liters/minute with little or no drawdown. The limit is by the size of the well and pump and not by the physical properties of the aquifer. This is because of the karst environment of south-central Texas with extensive conduits being common (Schindel et. al., 2007).

The Edwards Aquifer is primary for supplying domestic water for over one million people in San Antonio, is the major source of potable water for Bexar County, and supplies other domestic, industrial, and agricultural needs for counties within the region. There are several major artesian springs that support recreational activities and businesses, provide flow to downstream users, and ensures the survival of several federally protected plant and animal species. The aquifer is extremely complex and dominated by fractured, faulted, karst formations.

Currently, the aquifer satisfies these water requirements although public water restrictions are common during drought periods. Despite the aquifer's vast storage capacity and transmissive capabilities, the next period of drought could result in economic and environmental hardships for the region.

The primary emphasis of this paper is to review the modeling techniques used by Maclay and Land (1988) and the evidence that was incorporated in modeling by Lindgren et. al. (2004). This review just touches on many of the refinements that were authored by several scientists. Even with my research, many more papers have been prepared that provide additional evidence for future modeling work, contamination, and the complexities. The evidence influences modeling for connectivity across faulting, effects of conduits, the heterogeneity of the karsts and caves, and

understanding contamination that relate directly to the citizens of San Antonio and the immediate surrounding area. First, we need to review the geologic history of the south-central Texas region.

2. Geologic History:

There are preserved remnants in the core of the Llano Uplift of a Proterozoic batholith complex. This complex is generally of positive relief since about 1.1 ga and is likely related to the Grenville province trend. Late in the Proterozoic, rifting to the southeast of the Llano region occurred as the Iapetus Ocean opened between North America, Europe, and Africa (Thomas, 1977).

During the Paleozoic and Mesozoic Era, the recognizable geography began to appear. First, during the Pennsylvanian Period, the Ouachita - Marathon contraction formed an orogenic recess around the Llano Uplift. The emergent event continued during the Permian and Triassic Period. The Ouachita orogeny is the last event after the Taconic, Acadian, and Allegheny orogeny (Ferrill et. al., 2005).

The subsidence began during the Jurassic Period with opening of the Gulf of Mexico basin. This basin event occurred through the Cretaceous Period. Then the Tertiary Period provided another emergent phase with continued subsidence and sedimentation during the regression event (Ferrill et. al., 2005).

The features that surround the San Antonio region were reefs and basins, both exposed and subsurface. The Lower Cretaceous rocks that comprise the Edwards aquifer were deposited upon the landward margin of the Comanche continental shelf which was sheltered from the storm waves and deep ocean by the Stuart City rudistid barrier reef trend in the ancestral Gulf of Mexico, forming the offshore margin of the Central Texas platform. Subsidence across a tectonic hinge line that skirted the southern edge of this carbonate shelf kept most of the Edwards Aquifer submerged within a curved bank of reefal growth known as the Devils River trend. Greater rates of subsidence

south of the hinge line caused fundamental differences between rocks deposited within the Devils River trend and those deposited in deeper water inside the Maverick Basin. These geological features are illustrated in Figure 1 (Clark et. al., 2006).

The San Marcos platform became the site of cyclic deposition with transgression and progradation in the San Antonio area. The Edwards Aquifer, within the San Marcos platform, formed from the lower Cretaceous limestone with lithologies from the Kainer and Person Formation with the overlying Georgetown Formation of the Edwards Group. The Georgetown Formation consists of stratigraphically distinct limestone but is generally of lower porosity and hydraulic conductivity but has a very karstic stratigraphy (Lindgren et. al., (2004). The Del Rio Formation has different lithology of reddish-brown, gray, to light tan, marly limestone and clay of varying colors overlying the Georgetown Formation. The Del Rio is relatively impermeable and confines the lower stratigraphic units. The confined beds for the base of the Edwards Aquifer are the Upper Glen Rose Limestone which is composed of a thick sequence consisting of marl, shale, and dolomite (Maclay and Land, 1988).

The final stage was the erosional hiatus of evaporite sedimentation cycle, deposited on the hot supratidal flats of the San Marcos platform. These deposits were wholly or partly removed by circulating ground waters and collapsed breccias of high porosity and permeability. Subaerial erosion removed about 100 ft or more of the deposits and resulted in karstification (Maclay and Land, 1988).

Subsidence of the Gulf Coast Region continued throughout the late Oligocene and early Miocene Epoch. This renewed extensional deformation occurred from about 30 ma to 15 ma resulting in the Gulf of Mexico we know today (Ferrill et. al., 2005) and the formation of the Balcones Fault Zone. The Edwards Aquifer is located along the Balcones Escarpment, a topographic feature that separates the Edwards Plateau and the Texas Hill Country from the Gulf Coastal Plain.

A lack of decollement horizon beyond the stratigraphic pinchout of the detachment horizon prevented propagation of the faulting into central and west Texas and formed the Balcones Fault System. The hydraulic gradient increased from 1500 ft uplift in the western region and 3400 ft downdip below sea level at the aquifer limit.

Viewing Table 1, the Edwards Group is equivalent to the Devils River Limestone; and the West Nueces, McKnight, and Salmon Peak Formations of the Maverick basin (Lindgren et. al., 2004).

3. Research and Results

Numerical Modeling

Reviewing the previous history, from 1981 to 1985 the main thrust of research has been directed toward testing and expanding hydrogeologic concepts. Maclay and Land (1988) developed a finite-difference model to refine the storage and flow concepts of the Edwards Aquifer. The model was calibrated with measured data for the period 1972-1976, and it was shown to predict springflows during this time adequately (McKinney and Sharp, 1995).

Lindgren et. al. (2004), prepared their report simultaneously. A FORTRAN computer-model code, MODFLOW (McDonald and Harbaugh, 1988; Harbaugh and McDonald, 1996; Harbaugh et. al., 2000), was used in conjunction with a modular finite-difference ground-water flow code developed by the USGS (2000-2003). Simplifying assumptions about the Edwards Aquifer and boundary condition specifications were required to make mathematical representation of the aquifer possible.

Worthington (2003) estimated the location of the major high conductivity conduits from evidence within the Edwards Aquifer. Lindgren et. al. (2004) updated the model with these modifications and generated the figures of simulated hydraulic heads, cell-by-cell flows, and water budget. Schindel et. al. (2005) and Hovorka et. al. (2004) have conducted tracer tests identifying additional convergent conduits.

Steady-State and Transient Simulations

Lindgren et. al. (2004) performed the steady state modeling calibration period for 1939-46. This period was chosen because this time period provided useful analysis conditions. The measured water-level altitude of the potentiometric surface for the period and the modeled results of the simulation program are available for review in Lindgren et. al. (2004).

The transient simulation included changes in ground-water storage over time that result from pumping and other hydraulic stresses. The simulated flow directions and the estimations from the evidence by Worthington (2003) for the possible conduit locations for February 1975 may be reviewed in the paper by Lindgren et. al. (2004).

Fractures and Faulting

Fractures, unconformable contacts, and voids are common throughout the entire thickness in the Edwards Group. Many fractures cross several strata, although many are discontinuous or partially closed within massive-bedded dense mudstones. Unconformable contacts occur within the Edwards Group representing periods of subaerial erosion and cavernous porosity (Maclay and Land, 1988).

The high permeability is a result of dissolution imprinted upon zones of weakness, such as fractures, faults, bedding plane partings, and stratigraphic features (Schindel et. al., 2007)There are a few dozen faults with displacements greater than 15 m (49 ft) that are mappable, but only a small number have sufficient displacement to fully separate the Edwards limestones. The Haby Crossing fault, with a displacement greater than 150 m (500 ft), the most dominant fault throw within Bexar County, offsets the Edwards Group with the Glen Rose Formation (Ferrill et. al., 2005).

Ferrill et. al. (2005) quantified the influence of water movement through the (1) fault throw, (2) thinning by fault displacement, and, (3) the potential for distributed deformation or smear from the

confined beds. Preparation of three 7.5" USGS Quadrangles in north Bexar County with fault length and displacement provided an understanding fault influence.

Faults in the Balcones Escarpment provide greater understanding since Lindgren et. al. (2004) performed their numerical simulations. The increase in knowledge should be a part of any future modeling work.

Conduit, Karst, and Cave Hydrogeology

The Edwards Aquifer has some very unusual characteristics. First, drilling highly productive wells in the artesian zone is most unusual due to the intersection of conduits. Second is the unusual extreme depth for circulation of fresh water in the Edwards Aquifer. Third is the abrupt change in yields and water quality across the Bad Water Line. This characteristic also remains largely un-investigated and unexplained. Recharge enters the artesian zone of the aquifer, and the diffuse hypogene sponge work porosity of the aquifer allows for high yielding wells with limited drawdown and a complex natural spring system. (Schindel et. al., 2007). Significant heterogeneity is observed with flow conduits in the Edwards Aquifer. Recent tracer tests of northern Bexar County (Schindel et. al., 2005), Barton Springs (Hovorka et. al., 2004), and others illustrate the complexity.

Caves also provide important but incomplete information about the characteristics of epigenic conduits (Schindel et. al., 2007). Interestingly enough, Lindgren et. al. (2004) stated that consideration might be given to the free-cascades, waterfalls, or underground streams that are common within these cave areas. Identifying all the subsurface caves are still a problem but are very important in the estimations of heterogeneous connectivity. Also, electrical conductivity measurements imply that a conduit may exist parallel to the freshwater/saline-water interface (Worthington, 2003).

Deep hypogenic conduits are known from (1) borehole televiewer images of caves, (2) cave textures and sediments recovered in cores, (3) bit drops during well construction, (4) oversize caliper logs, and, (5) off scale porosity logs. The principal evidence of flow through karst is the heterogeneous and rapidly responsive nature of water-level variation (Lindgren et. al., 2004).

More understanding of conduits, karst influence, and caves within the aquifer needs to be considered in future numerical simulations.

Tracer Tests

Integrating and comparing the suite of conduit indicators will give an increase in density of these difficult conduits. These notches, troughs, or inferred conduits provide connectivity across the Trinity-Edwards confined bedding and across barrier faults. From this data density obtained from measurement, effort will be defining the narrow conduit locations. The hypothesis once was that small conduits make up only a fraction of the rock and larger conduits much less (Hovorka et. al., 2004). An estimate of the conduits, based on evaluation of the data, were previously defined by Worthington (2003) and modeled by Lindgren et. al. (2004). Recent tracer tests have indicated that conduits may be more wide spread than originally thought.

There is evidence from the tracer tests that conduits provide cross-formational interconnection across fractured and confined boundaries (Schindel et. al., 2005). By 2005, dye injected at points in vertical caves below the Glen Rose Formation showed a preferential flowpath associated with Panther Springs Creek basin (north Bexar County). Caves (Figure 3) in north Bexar County are behind the footwalls of barrier faults and penetrates the lower confined bedding of the Glen Rose Formation. The conduit velocity for three of these caves ranged from 5400 to 13,300 ft/day (Figure 4) showing hydraulic connection in Figure 5 (Schindel et. al., 2005). Note the horst formed where Loop 1604 is located. Both the north and south faults exceed the 100 m barrier designation, offsetting the Kainer and Person Formations.

Previously, the confined bedding was supposedly limited by small to moderate permeabilities of the Basal Nodular Member and the Dolomitic Member (Table 1). The recorded velocities (Figure 4, 5) identify the overprint confirming hydraulic connectivity across confined beds and through previously modeled barrier faults. Panther Springs Creek, as an additional conduit, should be added requiring an overprint on the Worthington (2003) characteristic estimates in future modeling techniques.

Western Edwards Aquifer Boundary Changes

Another concern which definitely affects modeling work is a contract study released which redefined the western aquifer boundary. The purpose of this study was to (1) model the groundwater systems in Uvalde County and (2) clearly define the hydrogeologic relationship between the Kinney County basin, the Uvalde sub-basin, and the San Antonio pool of the Edwards Aquifer. This study included all of the principal aquifers in Uvalde and Kinney counties. The paper by Green et. al. (2006), pages 35-36, shows the geographic locations of these pools and basins.

Previous work stated that the recharge captured in Kinney County flows from west to east into Uvalde and San Antonio pool area. Green et. al. (2006) analysis of the recent evidence identified that the Kinney County basin is separate from the San Antonio pool and Uvalde sub-basin. An embayment in the base of the Edwards Aquifer in the Grass Valley area supports the hypothesis that groundwater in the Kinney County basin flows to the southwest, generally exiting Las Moras Springs and the Leona River flood plain near Brackettville. The Kinney-Uvalde County line is now the new western boundary of the aquifer. Prior to this study, the old western boundary was located in western Kinney County and the groundwater flow was assumed to flow from west-to-east (Green et. al., 2006).

The Knippa Gap in east-central Uvalde County dams the groundwater flow and greatly decreases hydraulic conductivity to the San Antonio pool, defining in the Uvalde sub-basin. This explains why

the change of 10-15 ft is common in Uvalde while the groundwater elevations change 65-80 ft to the east of the Knippa Gap in the San Antonio pool during a combination of rainfall events in the Edwards Aquifer (Green et. al., 2006).

Water Quality and Contamination

The threat to San Antonio is that the increasing development upon the recharge zone could be detrimental to the quality of the water entering the Edwards Aquifer (Clark, 2000). Concern must be taken that the groundwater could be contaminated by spills or leaks of waste materials, particularly fluids associated with runoff from rapidly developing urban areas and leachate from septic tanks (Clark, 2000).

Available data for the Edwards Aquifer recharge zone were entered into a digital spatial database. Aerial photographs were used to help identify geologic landmarks. The process adapted for generating the vulnerability map (Figure 6) were (1) hydrogeologic units, (2) faults, (3) caves - sinkholes, (4) slopes, and (5) soils. Table 2 also references possible members and formations with a karstic characteristic (Clark, 2000).

The ground–water vulnerability map was generated based on the cumulative ratings of all selected natural features. The cumulative ratings ranged from 16 to 135. The majority of the 350,577 total cells were ranked between 26 and 66. The cumulative ratings from 26 to 56 were the result of the effects of the hydrogeologic unit, slope, and soil. Cells that were between 56 and 66 also have the effect of sinkholes plus the previous three characteristics (Clark, 2000).

After the vulnerability map was complete, three methods were used to assess the vulnerability of ground water to contamination in the recharge zone. These three concepts were (1) to assess before land plots can be developed, (2) evaluate the environmental impacts, and, (3) to evaluate ground-water pollution potential of any hydrogeologic setting with existing data (Clark, 2000).

4. Conclusions

Significant progress has been made with modifications to the finite-difference modeling software used by Maclay and Land (1988). Revisions in the numerical model were used to simulate flow in the San Antonio region of the Edwards Aquifer (Lindgren et. al., 2004). Questions arose with additional testing and analysis between 2004 and 2007 as how to best incorporate velocities from conduits that cross-cut barrier faults and flow paths that penetrate confined bedding (Schindel et. al., 2005).

The analysis for the Edwards Aquifer model indicated that the simulated hydraulic heads and spring flows are sensitive to variations in the storativity**.** An initial assumption was made but was based on a general lack of data**.** Additional research is needed on how storativity could be estimated on the basis of known or measurable rock properties and burial depth**.**

Excellent work has been accomplished establishing narrow converging conduits in Panther Spring Creek (Schindel, et. al., 2005) and Barton Springs (Hovorka et. al., 2004) as well as others. The tracer tests that have been conducted have been somewhat limited because of the number of wells and their locations. Because of the heterogeneous hydraulic conductivity, caves are also important for researching possible conduits in the future. These efforts are ongoing and continue to provide excellent results for additional modeling efforts.

Research work was completed in 2006 that accurately defined boundaries and located basins and sub-basins in the western portion of the Edwards Aquifer. Primarily, the research was dependent on gaining access to many wells that were superimposed on the Edwards Aquifer Authority monitored wells (Green et. al., 2006). Effort should be undertaken for the addition of adequate wells to more accurately define these characteristics throughout the Edwards Aquifer San Antonio region and continue the modeling work conducted by Lindgren et. al. (2004).

Study results indicate that the southeastern region of the recharge zone of the Edwards Aquifer is most susceptible to contamination because of population and geologic features. Figure 6 is intended for planning purposes (Clark, 2000).

Improvements in modeling, karst environments, conduits, and other geologic features should be used for a number of reasons. Two concerns are to protect overuse by San Antonio population and for the planners and regulators taking heed from pollution and contamination (Figure 6) as population explodes above the recharge zone. San Antonio's future growth and survival depends on supply and quality of the Edwards Aquifer protecting our primary water source in the future.

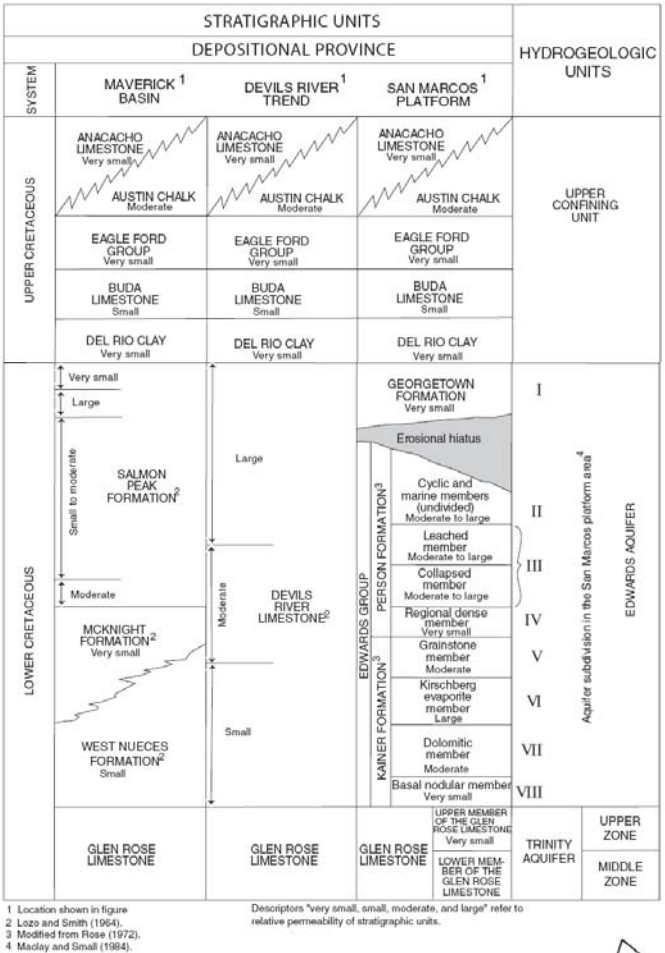

Table 1: Correlation of Cretaceous stratigraphy, hydrogeologic units, and permeabilities for the Edwards Aquifer region, Texas

(Lindgren et.al., 2004; modified from Maclay, 1995, fig. 11)

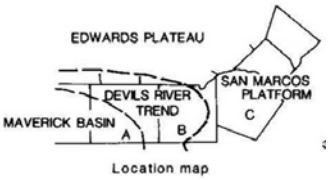

figure

[Hydrogeologic subdivisions modified from Maclay and Small (1976); groups, formations, and members modified from Rose (1972); lithology modified from Dunham (1962); and porosity type modified from Choquette and Pray (1970). CU, confining unit; AQ, aquifer]

Hydrogeologic subdivision			Group, formation, or member			Hydrologic function	Thickness (feet)	Lithology	Field identification	Cavern development	Porosity/ permeability type
Upper Cretaceous	Upper confining unit		Eagle Ford Group			CU	30–50	Brown, flaggy shale and argillaceous limestone	Thin flagstones; petroliferous	None	Low porosity/low permeability
			Buda Limestone			CU	40–50	Buff, light-gray, dense mudstone	Porcelaneous limestone with calcite-filled veins	Minor surface karst	Low porosity/low permeability
			Del Rio Clay			CU	40–50	Bluish-green to yellowish-brown clay	Fossiliferous; *Ilymatogyra arietina*	None	None/primary upper confining unit
Lower Cretaceous	I	Edwards aquifer	Georgetown Formation			Karst AQ; not karst CU	2–20	Reddish-brown, gray to light-tan, marly limestone	Marker fossil; *Waconella wacoensis*	None	Low porosity/low permeability
	II		Edwards Group	Person Formation	Cyclic and marine members, undivided	AQ	80–90	Mudstone to packstone; *miliolid* grainstone; chert	Thin graded cycles; massive beds to relatively thin beds; crossbeds	Many subsurface; might be associated with earlier karst development	Laterally extensive; both fabric and not fabric/ water-yielding
	III				Leached and collapsed members, undivided	AQ	70–90	Crystalline limestone; mudstone to grainstone; chert; collapsed breccia	Bioturbated iron-stained beds separated by massive limestone beds; stromatolitic limestone	Extensive lateral development; large rooms	Majority not fabric/one of the most permeable
	IV				Regional dense member	CU	20–24	Dense, argillaceous mudstone	Wispy iron-oxide stains	Very few; only vertical fracture enlargement	Not fabric/low permeability; vertical barrier
	V			Kainer Formation	Grainstone member	AQ	50–60	*Miliolid* grainstone; mudstone to wackestone; chert	White crossbedded grainstone	Few caves	Not fabric/recrystallization reduces permeability
	VI				Kirschberg evaporite member	AQ	50–60	Highly altered crystalline limestone; chalky mudstone; chert	Boxwork voids, with neospar and travertine frame	Probably extensive cave development	Majority fabric/one of the most permeable
	VII				Dolomitic member	AQ	110–130	Mudstone to grainstone; crystalline limestone; chert	Massively bedded light gray, *Toucasia* abundant	Caves related to structure or bedding planes	Mostly not fabric; some bedding-plane fabric/ water-yielding
	VIII				Basal nodular member	Karst AQ; not karst CU	50–60	Shaly, fossiliferous, nodular limestone; mudstone; *miliolid* grainstone	Massive, nodular and mottled, *Exogyra texana*	Large lateral caves at surface; a few caves near Cibolo Creek (see pl. 1)	Fabric; stratigraphically controlled/large conduit flow at surface; no permeability in subsurface
	Lower confining unit		Upper member of the Glen Rose Limestone			CU; evaporite beds AQ	350–500	Yellowish-tan, thinly bedded limestone and marl	Stair-step topography; alternating limestone and marl	Some surface cave development	Some water production at evaporite beds/relatively impermeable

Table 2: Summary of the lithologic and hydrologic properties of the hydrogeologic subdivisions of the Edwards Aquifer recharge zone, Bexar County, Texas
(Clark, 2000)

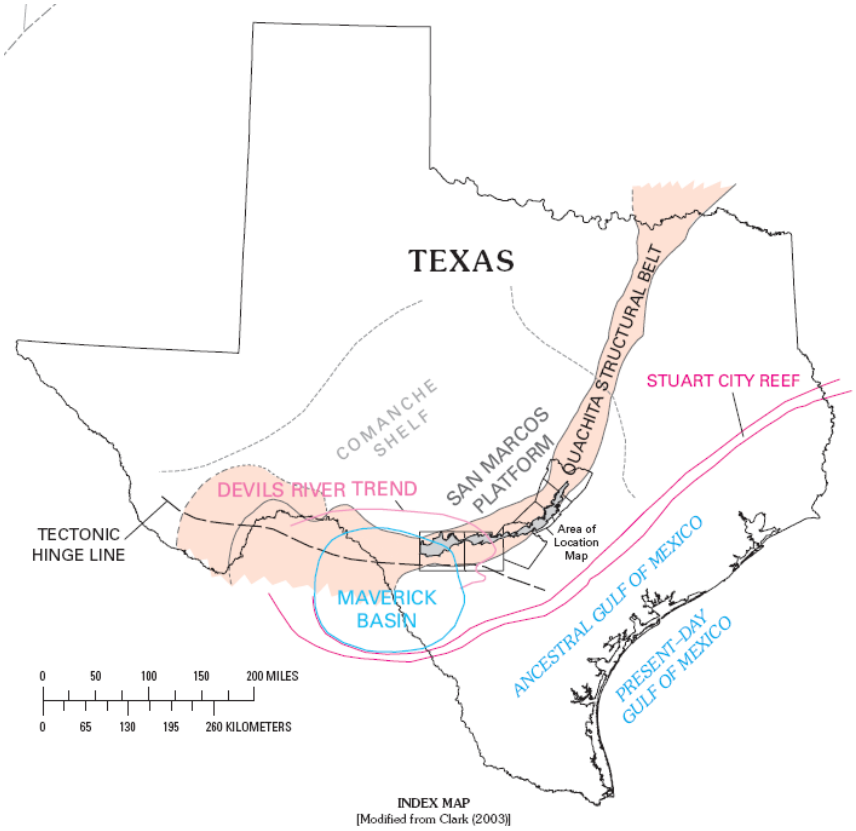

Figure 1: Paleogeographic and structural features in Texas associated with the Edwards Aquifer
(Clark, 2003)

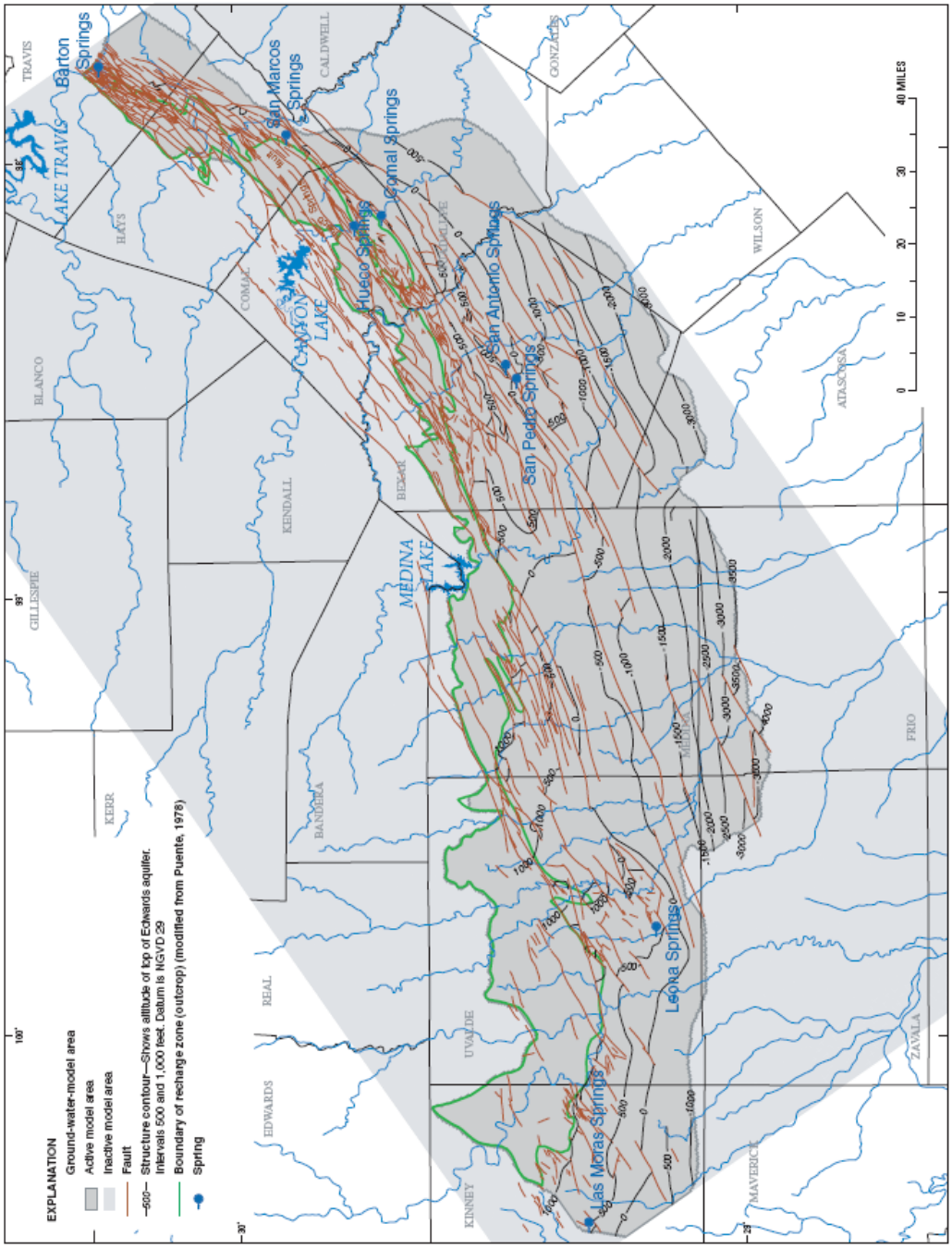

Figure 2: Map of the Balcones Fault System in the San Antonio area. Note that the depth to the top of the Edwards Aquifer is indicated on the map (Datum NAVD 29).

Note: This illustration locates the counties mentioned within this report

(Ferrill et.al., 2005; modified from Collins and Hovorka, 1997)

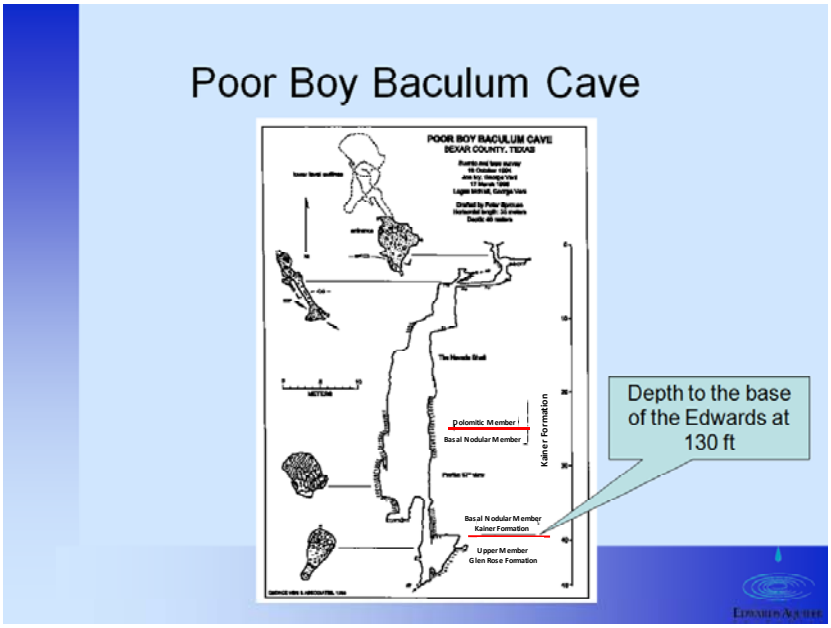

Figure 3: Cross-section of Poor Boy Baculum Cave located within Camp Bullis near San Antonio, Texas. A tracer dye was injected in the confined bedding of the Glen Rose Formation behind a barrier fault in order to understand the hydraulic connectivity between the Trinity Aquifer and the Edwards Aquifer and to cross-flow the fault. The ground-water flow velocity was extremely high, ranging from 6900 ft/day to 11,600 ft/day

(Schindel et.al., 2005)

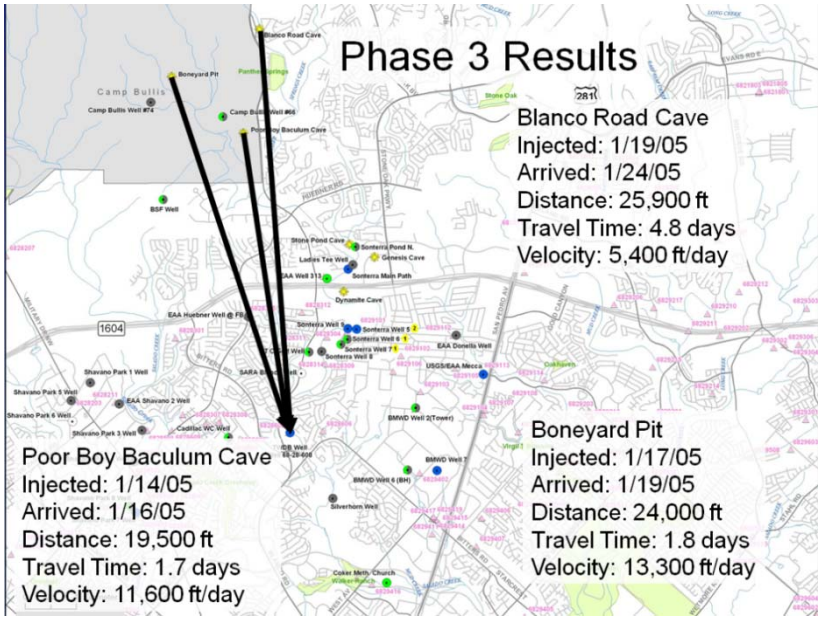

Figure 4: Tracer test locations parallel to Panther Spring Creek in northern Bexar County, Texas. Phase 3 indicates that these three caves all have very high velocities, illustrating a trough that translates from the Trinity into the Edwards Group, providing barrier fault cross-flow.

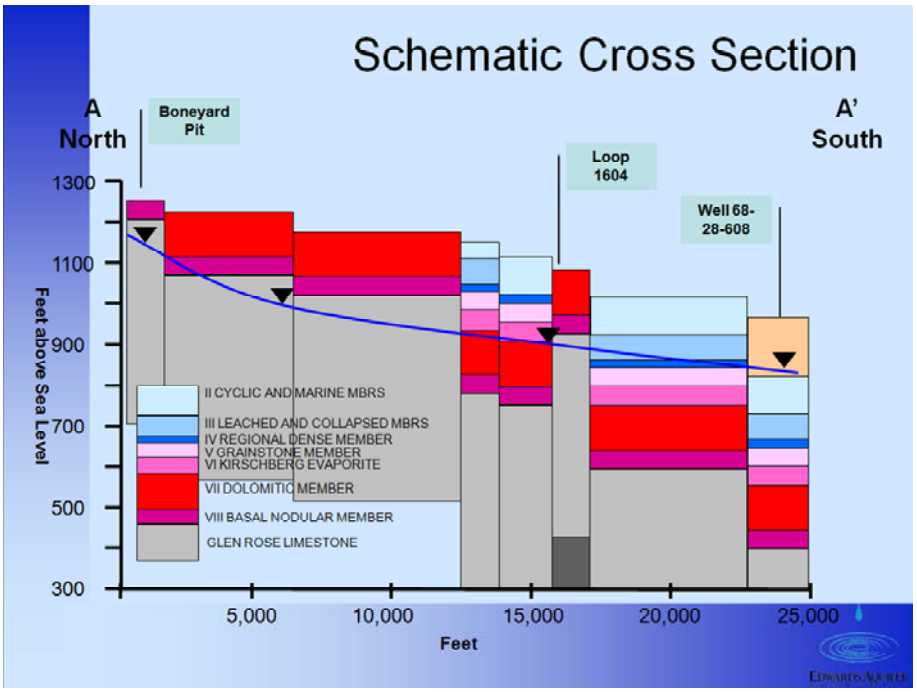

Figure 5: (B) Phase 3 indicates these three caves penetrate the lower confined bedding and the barrier fault footwall with very high velocitities. This illustrates possible trough connection across both geologic features.
(Schindel et.al., 2005)

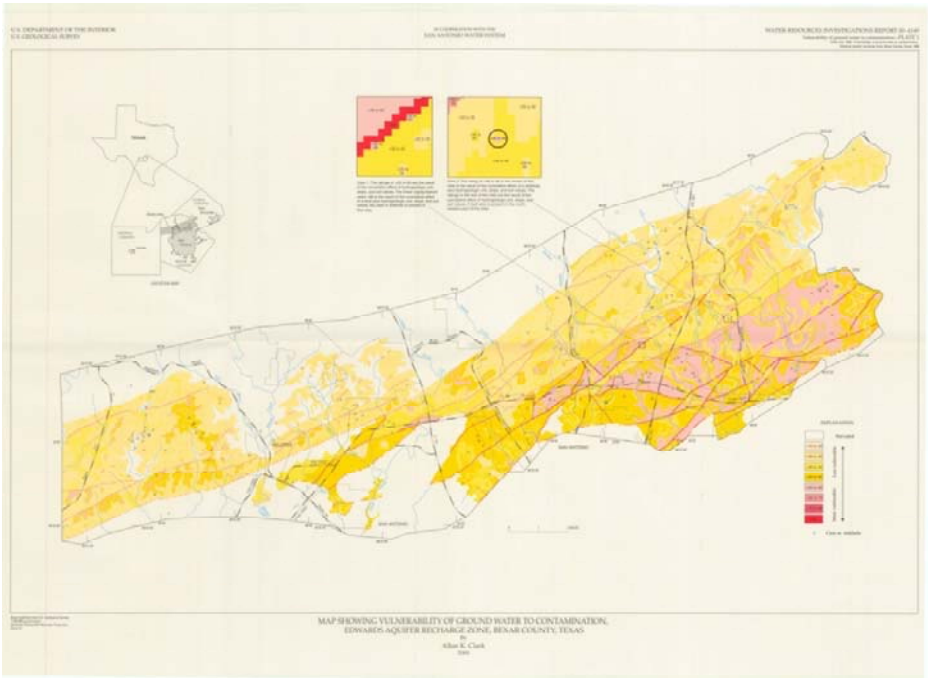

Figure 6: Map showing vulnerability of ground-water to contamination, Edwards Aquifer recharge zone, Bexar County, Texas
(Clark, 2000)

References Cited:

- Clark, A.K.; 2000; Vulnerability of ground water to contamination, Edwards Aquifer recharge zone, Bexar County, Texas, 1998: U.S. Geological Survey Water Resources Investigations Report 00-4149; 9 pgs.

- Clark, Allan K.; 2003; Geologic framework and hydrogeologic characteristics of the Edwards Aquifer, Uvalde County, Texas; U.S. Geological Survey, Water Resources Investigations Report 03-4010; 17 pgs.

- Clark, Allan K.; Faith, Jason R.; Blome, Charles D.; Pedraza, Diana E.; 2006; Geologic Map of the Edwards Aquifer In Northern Medina and Northeastern Uvalde Counties; U.S. Geological Survey, Open-File Report 2006-1372; 22 pgs.

- Ferrill, David A.; Morris, Alan P.; and Waiting, Deborah J.; 2005; Structure of the Balcones Fault System and architecture of the Edwards and Trinity Aquifers, South-Central Texas; Geological Society of America South-Central Meeting Spring 2005; 39 pgs.

- Green, Ronald T.; Bertetti, F. Paul; Franklin, Nathan M.; Morris, Alan P.; Ferrill, David A.; and Klar, Richard V.; 2006; "Evaluation of the Edwards Aquifer in Kinney and Uvalde Counties, Texas": Contract report by Southwest Research Institute to Edwards Aquifer Authority, 113 pgs.

- Hovorka, S.D.; Phu, T.; Nicot, J.P.; and Lindley, A.; 2004; Refining the conceptual model for flow in the Edwards aquifer – Characterizing the role of fractures and conduits in the Balcones fault zone segment: Contract report to Edwards Aquifer Authority, 53 pgs.

- Lindgren, R.J.; Dutton, A.R.; Hovorka, S.D.; Worthington, S.R.H.; and Painter, S.; 2004; Conceptualization and Simulation of the Edwards Aquifer, San Antonio Region, Texas; U. S. Geological Survey, Scientific Investigations Report 2004-5277, 143 pgs.

- Maclay, R.W.; and Land, L.F.; 1988; Simulation of Flow in the Edwards Aquifer, San Antonio Region, Texas, and Refinement of Storage and Flow Concepts; U. S. Geological Survey Water-Supply Paper 2336-A, 48 pgs.

- McKinney, Daene C.; Sharp, Jr., John M.; 1995;Springflow Augmentation of Comal Springs and San Marcos Springs, Texas: Phase I – Feasibility Study; Center for Research in Water Resources, Buereau of Engineering Research, The University of Texas at Austin; Technical Report CRWR 247, pg. 5.5.

- Schindel, Geary; Johnson, Steve; Veni, George; and Schnitz, Lew; 2005; Tracer tests in northern Bexar County Edwards Aquifer recharge zone: Panther Springs Creek Groundwater Basin; internal EAA presentation.

- Schindel, Geary M.; Johnson, Steve; and Alexander Jr., E. Calvin; 2007; Hypogene Processes in the Balcones Fault Zone Edwards Aquifer in south-central Texas, a new conceptual model to explain

aquifer dynamics; Edwards Aquifer Authority Stratigraphy Field Trip, October 5 and 6, 2007; subset of internal EAA document.

- Thomas, W.A.; 1977; Evolution of Appalachian-Ouachita salients and recesses from reentrants and promontories in the continental margin; American Journal of Science, v. 277 no. 10; pgs. 1233-1278.

- Worthington, S.R.H.; 2003; Conduits and turbulent flow in the Edwards aquifer: Worthington Groundwater, contract report to Edwards Aquifer Authority, San Antonio, Tex. 41 pgs..

MODIS-based snow cover variability of the Upper River Grande Basin

Beibei Yu , Xianwei Wang , Hongjie Xie

Laboratory for Remote Sensing and Geoinformatics

University of Texas at San Antonio, Texas 78249, USA

Abstract

Snow cover and its spring melting in the Upper Rio Grande Basin provides a major water source for the Upper to Middle Rio Grande valley and Elephant Butte Reservoir. Thus understanding the snowpack and its variability in the context of global climate change is crucial to the sustainable water resources for the region. MODIS instruments (on Terra and Aqua) have provided time series of snow cover products since 2000, but suffering with cloud contaminations. In this study, we evaluated four newly developed cloudless snow cover products (less than 10%) and four standard products: daily (MOD10A1, MYD10A1) and 8-day (MOD10A2, MYD10A2), in comparison with *in situ* Snowpack Telemetry (SNOTEL) measurements for the hydrological year 2003-2004. The four new products are daily composite of Terra and Aqua (MODMYD10DC), multi-day composites of Terra (MOD10MC), Aqua (MYD10MC), and Terra and Aqua (MODMYD10MC). The standard daily and 8-day products can classify land correctly, but daily products had fairly low accuracy in snow classification due to cloud contamination (a average of 39.4% for Terra and 45% for Aqua) and 8-day products tended to overestimate the snow cover and have a much reduced temporal resolution.All the new multi-day composite products tended to have higher accuracy (about 78% for the

hydrological year and 83% for winter season) than the daily product, as the cloud cover has been reduced to less than 10% (~5% for the year) under the new algorithm . This result is consistent with a previous study in the Xinjiang area, China (Wang and Xie, 2007). Therefore, MODMYD10MC products are used to get the mean snow cover of the Upper Rio Grande Basin from 2000 to 2007. The change of the mean snow cover showed an unexpected fluctuated trend rather than continuously decrease due to global warming.

Key words: Snow cover; Grande Rio Basin; multi-day composite; MODIS; SNOTEL

1. INTRODUCTION

Snow has a major impact on the Earth's energy balance because of its high albedo and low thermal conductivity, and also has a major influence on atmospheric circulation by modifying overlying air masses. Since snow is held in cold storage on a basin for an extended period of time before it enters the runoff process, thus, there is such a vast difference in the physical properties of snow and other natural surfaces that the occurrence of snow on a drainage basin can cause significant changes in the energy and water budgets. As an example, the relatively high albedo of snow reflects a much higher percentage of incoming solar short wave radiation than snow-free surfaces (80% for relatively new snow as opposed to roughly 15% for snow-free vegetation). Snow may cover up to 53% of the land surface in the northern hemisphere and up to 44% of the world's land areas at any one time. Because so much of the water supply used by humans comes from snow cover, especially in mountainous areas throughout the world, snow water equivalent (SWE) is a critical snowpack parameter. However SWE cannot yet be

measured remotely with the accuracy required by hydrologic models. (Dorothy K. Hall 2007)To obtain accurate SWE estimates from space, other sources of information, including station data and snow-covered area, should be used, together, to increase their usability in land-surface models.

Snow-cover maps of the Northern Hemisphere have been available since 1966 from the National Oceanic and Atmospheric Administration (NOAA). (Hall *et al.* 2002) Snow cover can be detected and monitored with a variety of remote sensing devices. The greatest numbers of applications have been found in the VNIR region of the electromagnetic spectrum. NOAA polar orbiting satellite with the AVHRR, which has a resolution of about 1 km has been used by many researchers to detect snow. The frequency of coverage is twice every 24 h (one daytime pass and one nighttime pass). The major problem with the NOAA-AVHRR data is that the resolution of 1 km may be insufficient for snow mapping on small basins. On December 18, 1999, the Earth Observing System (EOS) Terra spacecraft was launched with a complement of five instruments, one of which is the Moderate Resolution Imaging Spectroradiometer (MODIS). (Hall *et al.* 2002) Data from the MODIS instrument with 500 m resolution will partially alleviate this problem. In this study, MODIS data is used. However, Cloud blockage, particularly when snow covers the land surface in the winter months, seriously impairs the application of MODIS snow cover products. (Tekeli *et al.* 2005)

Daily product (MOD10A1, MYD10A1)

The MODIS snow daily product has a higher commission error than omission error, especially for dense forests (Klein & Barnett, 2003 and Simic et al., 2004). When comparing the MODIS daily product with NOHRSC product, the general conclusions derived from these validation studies are: (1) the MODIS daily snow-cover product misclassifies fewer snow pixels; (2) the MODIS daily product classifies fewer cloud pixels, especially in the forested areas; (3) the MODIS daily product classifies more snow pixels in forested areas than does the NOHRSC product; (4) the MODIS daily product has lower misclassification rate than the NOHRSC product, especially in more topographically complex and heavily forested basins such as the Upper Rio Grande River and Columbia River basins than basins that have less relief and less forest such as the Missouri River basin..(Zhou *et al.* 2005) Both snow and land are highly misclassified as cloud. A lot of cloud data were seen in the MODIS daily product. They concluded that for clear-sky days, the MODIS daily algorithm works quite well, especially for land-to-land classification. The major error seems to result from the misclassification of snow as land.

8 day product (MOD10A2, MYD10A2)

An 8-day composite maximum snow-cover product is produced for each tile by compositing 8 days of the daily 500-m resolution products. Eight-day periods begin from the first day of each year. (Hall et al, 2002). The classification accuracy of snow (SNOTEL) as snow or land as land by the MODIS 8-day product algorithm is generally high. The omission error of classifying snow (SNOTEL) as land or as cloud (MODIS) is relatively low or very low (1.6–11.7% for snow-as-land or 1.6–4.2% for snow-as-cloud).

The commission error of classifying land as snow is 2.1–15.1% and omission error of classifying land as cloud is 0.0–5.4%. (Zhou *et al.* 2005)

A limitation of the MOD10A2 is that persistent cloud cover over consecutive days or all days of the period can hide snow cover that may have existed during some or all of the period. For example, if the clouds responsible for a snow event do not clear before the end of the compositing period, then snow cover will not be mapped during the 8-day period during which it fell. In that situation the MOD10A2 product will show, erroneously, bare ground for that area, assuming there was no snow visible before that late-period snowfall.

Composite am-pm images

It is often not an easy task to collect a time-series of cloud-free images for a particular area of interest using MODIS, thus limiting its capability of mapping the snow cover accurately. A cloud-covered area in the morning may not be absolutely cloud-covered in the afternoon. Thus, a model to combine the am and pm images has been developed. According to Wang's algorithm, the strategy of combining two input images into one image is based on a prioritization scheme. Snow (200) has the first priority; Lake ice (100) has the second priority; Water body (37) has the third priority, Land/forest (25) has the fourth priority; The cloud (50) has the last order. In this case, if a pixel value in either input image is 200, then the pixel value in the combined image will be 200. If one of the input is 37, and the other is 50, the combined image will be 37. The rest may be deduced by analogy. If a pixel value is 255 (representing 0, 1, 244, and 255) in both input

images, or if the pixel value in one image is 255 and the other being 50, the pixel value will be assigned as 255 (no data) in the new image, which usually accounts for less than 0.05% of all pixels.

Multi-day composite images

Besides combining the morning and afternoon images, a further solution is to composite multiple daily snow cover images to produce a maximum snow cover image and thereby minimize short-term environmental contaminations, like cloud, aerosol, etc. (King et al., 1992), with a scarification of a reduced temporal resolution. The new algorithm and automated scripts developed by Wang et al, producing multi-day Terra (am) or Aqua (pm), and Terra-Aqua (am-pm) snow cover image composites, with flexible starting and ending dates and a user-defined cloud cover threshold, are used to produce cloud-less daily snow cover images and more cloud-free multi-day snow cover composite images than any single type (Terra or Aqua) of multi-day image composites. In order to achieve an image with the cloud cover less than 10%, 3 models were used. Besides the 4 standard MODIS data (MOD10A1, MYD10A1, MOD10A2, MYD10A2), four new products were generated: multi-day am composite images (MOD10MC), (2) multi-day pm composite images (MYD10MC), (3) daily am-pm composite images (MODMYD10DC), and (4) multi-day am-pm composite images (MODMYD10MC).

The largest factor affecting the accuracy of the MODIS snow products is snow cloud confusion. Specially, the cloud mask tends to map more clouds than are really

present. (Hall et al, 2007). Much of the discrepancy between MODIS snow cover estimates and the in situ SNOTEL observations occurs during the beginning and end of the snow season when thin snowpack conditions prevail.(Klein & Barnett 2003) The new algorithms are used in this study to combine morning and after images, as well as daily images to multi-day images, expecting to reduce the influence of cloud cover. Snow cover maps produced by MODIS data were compared with *in situ* Snowpack Telemetry (SNOTEL) measurements for the 2003-2004 snow season. Snow water equivalent was used to see how the snow depth might affect the accuracy. The aim of this study is to validate these 8 MODIS products, and find out the most representative product for mapping the snow cover. And then the trend of the snow cover area on the Upper Rio Grande Basin can be generated based on this MODIS product.

Study area

The Upper Rio Grande basin stretches 1885 miles, lying between the headwaters of the Rio Grande in the San Juan Mountains of Colorado and Fort Quitman, Texas.(Figure 1). The upper basin covers approximately 36,000 mi2 (92,000 km2) in southern Colorado, New Mexico and west Texas. It is bounded on the west by the United States Continental Divide and on the east by the Sangre de Cristo Mountain Range and a series of smaller ranges running generally north-south through the state of New Mexico.(Bella *et al.* 1996) Elevations range from over 14,000 feet (4267 m) to less than 4,000 feet (1219 m). The mainstem of the upper Rio Grande is about 725 miles (1160 km) long. The Upper Rio Grande is a typical example of river basins in semi-arid environments. The water resources of the basin include both surface and groundwater.

River flows are maintained mostly by seasonal precipitation. Spring snowmelt and summer monsoon storms are the main sources of surface flows and for groundwater recharge. The basin provides water for flora, fauna, agriculture, domestic consumption, recreation, business and industry. Agricultural and pastoral irrigation depends solely on the water derived from the river directly from the Rio Grande and its tributaries or indirectly from surface water in the reservoirs, or ground water supplies which are recharged from the river. Expanding urban populations along the Rio Grande River have also created growing demands for municipal and industrial uses of water.(Costigan *et al.* 2000) The Rio Grande River is highly regulated by reservoir systems, especially in the middle Rio Grande basin. However, compared to the lower portions of the river, the Upper Rio Grande River basin is relatively much more unregulated, pristine, and stable.(Zhou *et al.* 2005)

There are several reasons to choose the Upper Rio Grande Basin as a study area: First, snowmelt runoff represents an important water resource. Nearly all reaches of the Rio Grande are heavily utilized as a water resource. Downstream of the study region, the ground water resources in the Middle Rio Grande Basin, which supplies water to the Albuquerque metropolitan area, have been determined to be significantly less than previously believed [Thorn et al]. This will place additional pressure on the surface water supply from the Upper Rio Grande. Secondly, the Upper Rio Grande encompasses a large range of elevations, slopes and vegetation types and thus provides comparisons of satellite-derived snow cover maps and in situ observations over a wide range of environmental conditions while being of small enough extent to remain manageable. And the basin is sufficiently large for the medium resolution (250 m–1 km) of the MODIS

data but small enough for the management of data retrieval. Finally, Several snowmelt–runoff modeling studies have been carried out for the basin (e.g. Klein & Barnett, 2003, Rango & Martinec, 1994 and Rango & van Katwijk, 1990). These studies provide insights for the present evaluation study and results from the present study provide insights for future snowmelt–runoff modeling using remotely sensed snow products.(Zhou *et al.* 2005)

2. DATA SOURCES

MODIS

MODIS snow and ice products have been available through the National Snow and Ice Data Center (NSIDC). MODIS snow-cover products represent potential improvement to or enhancement of the currently available operational products mainly because the MODIS products are global and 500-m resolution, and have the capability to separate most snow and clouds. (Hall *et al.* 2002). First carried aboard the Terra spacecraft (passes the equator at about 10:30 am), which was launched on December 18, 1999, the Moderate Resolution Spectroadiometer (MODIS) began collecting science data on February 24, 2000. And a second MODIS instrument has been carried aboard the Aqua spacecraft (passes the equator in the early afternoon at about 1:30 pm) launched on May 4, 2002. MODIS is an environmental satellite operating in visible, near- and short-wave infrared and thermal portions of the electromagnetic spectrum. It is designed to provide global views of earth processes with its swath width of 2330 km enabling it to view the entire surface of the earth every 2 days.

Currently, there is no single means of assessing the performance of the MODIS snow cover products. No current operationally produced snow cover product is free enough from errors to serve as an absolute standard for comparison. Instead, ongoing validation of MODIS land products, including snow cover maps, are being accomplished through comparisons against in situ measurements, products derived from airborne and spaceborne sensors as well as through intercomparisons with other MODIS products and with process-based models [Morisette et al].

The MODIS instrument acquires images in 36 spectral bands between 0.405 and 14.385 μm, which depending on the spectral band have spatial resolutions of 250, 500 or 1000 m. The MODIS snow mapping algorithm utilizes the seven MODIS bands designed especially to image the land surface. Because the lowest spatial resolution of these bands is 500 m, snow discrimination and, consequently, the highest resolution MODIS snow cover products, are produced at a spatial resolution of 500 m. Most of the earth's snow-covered areas are imaged daily, with only snow cover at low latitudes being imaged every other day.

MODIS snow cover products (MOD10A1/A2) are a binary classification, which only can tell weather it is coved by snow or not, but can not measure how much snow it has, such as SWE, snow depth, etc. In the MODIS snow mapping algorithm, snow is distinguished from other surface covers by two primary distinguishing features. The first is its high reflectance in the visible wavelengths (MODIS band 4 at 0.545–0.565 μm) and second its low reflectance in the short-wave infrared (MODIS band 6 at 1.628–1.652 μm). (Hall et al., 2002) Normalized Difference Snow Index (NDSI) For MODIS is calculated as::

$$NSDI = \frac{Band\,4 - band\,6}{band\,4 + band\,6}$$

The snow detection algorithm for MODIS takes advantage of this unique spectral combination allowing for a fully automated and computationally frugal approach to snow detection. A pixel in a non-densely forested region will be mapped as snow if the NDSI is ≥0.4 and reflectance in MODIS band 2 (0.841–0.876 μm) is >11%. However, if the MODIS band 4 reflectance is <10%, then the pixel will not be mapped as snow even if the other criteria are met. This prevents pixels containing very dark targets such as black spruce forests, from being mapped as snow. (Hall, 2002) However, snow-covered forests may have lower NDSI values. To map these snowcovered forests better, a combination of the normalized difference vegetation index (NDVI) computed using MODIS bands 1 (0.620–0.670 μm) and 2 (0.841–0.876 μm) and the NDSI are used. Pixels falling in a polygon region in NDVI–NDSI space may be mapped as snow for NDSI < 0.4. However, to prevent very dark forests from being erroneously mapped as snow, the reflectance in MODIS band 4 must be greater than or equal to 10% even if other criteria are met. A split-window technique employing MODIS thermal bands 31 (10.780–11.280 μm)and 32 (11.770–12.270 μm) is used to mask misclassified pixels whose temperature is too high to contain snow.(Hall *et al.* 2002; Songweon Lee 2005)

In addition, MODIS snow products have three masks: thermal mask, cloud mask, ocean and inland water mask. Thermal Mask was introduced in October 2001 by a split-window techniques using MODIS infrared band 31 (10.78–11.28 μm) and band 32 (11.77–12.27 μm) (Key, et al., 1997). If the brightness temperature in a pixel is > 277k, then the pixel will not be flagged as snow, which eliminates much of the spurious snow cover, especially in warm areas (Hall, et al., 2002). Cloud Mask: The new cloud mask

was inserted in the data production system in September 2000. The MODIS snow algorithm reads the unobstructed field-of-view quality flag from the cloud mask. If that flag is set to 'certain cloud', then cloud is set in the snow cover algorithm. Any other setting of that flag is interpreted as a clear view of the surface (Hall, et al., 2002). Ocean and inland water mask was set up with the 1 km-resolution land/water mask contained in the MODIS geolocation product. The snow cover algorithm does not run on ocean waters, but does in inland waters, like in the Grate lakes (Hall, et al., 2002).

In this study, MODIS tiles h09v05and h09v05 cover the whole study area. MOD10A1, MYD10A1, MOD10A2, MYD10A2 from February 2000 through October 2007 were ordered through the EOS data gateway. They contain snow cover, snow albedo, fractional snow cover, and quality assessment (QA) data in a compressed HDF-EOS format along with corresponding metadata (Riggs et al, 2006). The MODIS snow cover image is a coded raster. Those coded integer values in the daily product include 0 (data missing), 1 (no decision), 11 (night), 25 (no snow), 37 (lake), 39 (ocean), 50 (cloud), 100 (lake ice), 200 (snow), 254 (detector saturated), and 255 (fill) (Riggs et al., 2006). In this study, 25 (no snow), 37 (lake), 100 (lake ice), 200 (snow) will be used and others will be classified as 255 (no data).

MOD10A2 is an 8-day composite product of snow cover that is made by compositing from 2 to 8 days of the MOD10A1 product. Eight-day periods begin on the first day of the year, continue consecutively and extend a few days (3 days for a regular year and 2 days for a leap year) into the next year. For the MOD10A2 8-day snow-cover product, the intent of the algorithm is to maximize the number of snow pixels while minimize the number of cloud pixels. A cell is labeled as cloud only when the pixel is

cloud-covered for all the 8 days. If snow cover is found for any of the 8 days, then the pixel in the "Maximum_Snow_Extent" Scientific Data Sets (SDS) is labeled as snow. (Zhou *et al.* 2005)

SNOTEL

The in situ measurements of snow depth were provided by the automated Snowpack Telemetry (SNOTEL) network maintained throughout the western states by the United States Department of Agriculture's National Resources Conservation Service (NCRS). Approximately 600 SNOTEL stations are scattered throughout 12 western states and Alaska, collecting information regarding temperature, precipitation, snow depth and snow water equivalent via a pressure sensing snow pillow for the purposes of forecasting water supply [Crook, 1977 and Natural Resources Conservation Service, 1997]. Essential characteristics both for hydrology and climatology include snow water equivalent (SWE) and snow depth (SD). Since the snow depth is not available in this case, SWE is used in the comparison. Snow Water Equivalent (SWE) is a common snowpack measurement. It is the amount of water contained within the snowpack. It can be thought of as the depth of water that would theoretically result if you melted the entire snowpack instaneously. (Pulliainen et al, 2005)

3. METHOD

A UNIX script is first developed to call the resample program to automatically convert the time series of daily or 8-day HDF-EOS files to GeoTIFF files. The output projection of UTM zone 13, with datum of WGS 84 is defined and a subset of a rectangle

area covering the Upper Rio Grande Basin is clipped during this procedure. An ArcInfo Arc Macro Language (AML) script is developed to batch convert the subset GeoTIFF files to Geographic Information System (GIS) grid format. The study area of the Upper Rio Grande Basin area is exactly clipped from the created grid files, and then a value-attribute table (VAT) of each grid is uploaded to a text file for further process and analysis. A multi-day composite image based on both Terra and Aqua daily images with flexible starting and ending dates as long as cloud cover reducing to less than 10% is generated based on the new algorithm developed by Wang et al.

Combination of Daily MOD10A1 or MYD10A1 Images

Two scripts, *mod_area.aml* and *myd_area.aml,* are used to combine the daily am-only MOD10A1 and pm-only MYD10A1 images, respectively. Both scripts are basically the same except for the naming setup of input and output images (the input of *mod_area.am* is daily morning images and the input of *myd_area.aml* is daily afternoon images). A user-defined percentage threshold of cloud cover (10% default) is applied to control the processes of multiple image composition. For example, if the cloud cover percentage of the input image 1 (either an originally daily image or a composite image) is less than the predefined threshold 10%, the compositing process stops, the image or the composite image outputs to a final product folder, and a new process of image composition is then started given images remaining in the folder. If cloud cover of the input image 1 is higher than 10%, the composite process continues. And this process stops only when the cloud cover percentage drops to lower than 10%. This model ensure that each final product has he cloud cover less than 10%.

Combination of Daily MOD10A1 and MYD10A1 Images

A script named *modmyd_area.aml* is developed to combine the MODIS Terra and Aqua daily snow cover products. The input images of *modmyd_area.aml* are one am image and one pm image. A cloud cover threshold of 10% is used as default. If the cloud cover of a composite image (input image 1) is ≥ 10%, another composite process is always needed, even if the second composite image (input image 2) has cloud cover less than 10%. The produced new composite image will have even less cloud cover than that of the input image 2. In this case, the image 2 itself is also copied to the final product folder.When the process comes to the end of MOD10A1 and MYD10A1 image lists, it will automatically terminate. Attention is required to be paid that the number of MOD10A1 image files and MYD10A1 image files should be equal, i.e., both images must be a pair on each day. If an am (or pm) image is missing, the corresponding pm (or am) image will be treated as for both am and pm images. (Wang et al)

Comparisons of each products were made against daily in situ snow water equivalent measurements made at 15 SNOTEL sites scattered at high elevations throughout the Upper Rio Grande River Basin. The comparison were completed in excel with VB scripts. A confusion matrix or error matrix is a generated to assess the accuracy of remotely sensed data.

4. RESULTS AND DISCUSSION

Validation of MODIS Products

Table 1 illustrates the comparison between all ground observations and MODIS snow cover daily morning product MOD10A1 at the 15 climatic stations in the 2003-04 hydrologic year There are total 2699 data of land (without snow) and 2626 data of snow

(SWE≥1 cm). In the 2699 in situ data of land/no snow, the MOD10A1g product misclassifies 40 of them as snow and 922 of them as cloud. The accuracy of land classification is 64%. The omission error classifying land as snow is 1% and as cloud is 34%. If the 922 cloud data pairs (corresponding to both MODIS and in situ) are removed from the calculation, the accuracy of land classification is 98% under clear sky conditions. The removal of the cloud data here (and hereafter) is only for comparison purpose under so-called clear sky conditions, and the accuracy of MODIS snow/land classification is not really improved.In the 2626 in situ observed data of snow, the MOD10A1 product misclassifies 364 of them as land and 1344 of them as cloud. The accuracy of snow classification is 35%. The omission error of classifying snow as land is 14% and as cloud is 51%. If the 1344 cloud data (pairs) are removed, the accuracy of snow classification increases to 72%, and the overall accuracy of MODIS land and snow classification increases from 50% to 87%.

Table 2 illustrates the comparison between all ground observations and MODIS snow cover daily afternoon product MYD10A1 at the 15 climatic stations in the 2003-04 hydrologic year. The omission error of classifying snow as cloud is even higher than the morning product, which may indicate that there is generally more cloud appear in the afternoon than in the morning. The land classification is as high as 99% under clear sky condition and only 23 pairs of data were misclassified as snow. The patch snow (SWE<1-4cm) and deep snow (SWE>=4cm) classification are 33% and 59% respectively, if the misclassified cloud is removed.

Compared to the results showed in table 1, Error matrix between MODMYD10MC and ground measurements in the 2003-04 hydrologic year at 15 stations on Rio Grande Basin showing in table 8 displayed a better result of classifying both land and snow. There are totally 2430 data, 1462 are land, and the others are snow. In the 1462 land data, 1330 were accurately classified as land, only 4% and 5% were misclassified as cloud and snow, respectively. Though the accuracy after cloud data is removed of the daily products is high, but the cloud in that case is statically removed. The multi-day am-pm composite products reduced the cloud cover to less than 10%, which provide us with better representative images.

The comparison between the winter season Multi-day am-pm composite products and SNOTEL SWE are showed in this table. The accuracy of the deep snow cover has increased from 78% to 83% (after cloud is removed).

Graph 1 shows the comparison results of 6 MODIS products validation. Generally, 3 of the multi-day composite products (MOD10A2, MYD10A2, and MODMYD10MC) have higher accuracy in overall, snow, as well as land classification than the daily products (MODA1, MYDA1, MODMYD10DC). The am-pm daily products display better results than the standard daily products. And all the products are good at classifying land pixels. Daily products show relatively low ability of classifying snow, which might because of very high percentage of total cloud. As we can see from the graph, those products, which have low total cloud, have higher accuracy in classifying both land and snow. In that case, snow is recognized as the biggest disturbance in the MODIS snow mapping work. MOD10A2 and MOD10A2, which are the MODIS 8 day products showed generally high

accuracy in classifying snow and their total cloud percentages are snow. However, MODIS 8-day composite product (MOD10A2) reduces the original temporal resolution of daily to 8 days, In algorithm of 8 day products, a pixel is classified as cloud only when the pixel is snow-covered in all the 8 days, but a pixel will be classified as snow even if there is only one day covered by snow. In that case, eight-day products tend to overestimate the snow cover, particularly in early or end of the snowfall periods when snow is easily melted away. In addition, the 8-day MODIS product using fixed starting and ending dates looses its flexibility in monitoring particular snowfall events. (Wang). Assuming the cloud condition detected by the cloud mask employed in both algorithms is the truth, eliminating the cloudy days in the comparison analysis shows that the MODIS daily algorithm works quite well or even better than the MODIS 8-day algorithm.

Mean Snow and Cloud Comparison Between MODIS products

The table above showed the results of the comparison between eight different products. MOD10A1 and MYD10A1 represent the standard morning and afternoon daily products, respectively. There are totally 356 morning images and 365 afternoon images. As 10 of the morning images are missing, only use 355 images were used for comparison (As a requirement for the new algorithm, the number of MOD10A1 image files and MYD10A1 image files should be equal). Based on those daily am and pm images, 350 daily am-pm composite images (MODMYD10DC) are generated. Showing in the table, the mean cloud cover of the standard daily morning product is as high as 39.5%, and even higher (45.1%) for the afternoon product. Clouds are the major cause for reduction of the overall accuracy of the MODIS daily product, which cause the mean snow cover of the afternoon

product come out fairly low (3.5%). These two products might underestimate the snow cover, due to the high cloud cover. Therefore, it is difficult to use these products for daily snow monitoring and forecasting. The daily am-pm composite images have annual mean cloud cover about 30.6%, which are 15% to over 20% less than the am or pm images. The multi-day composite image products generating under the new algorithm reduced the cloud cover to less than 10%. The new algorithm generated 129 multi-day am images, 111 multi-day pm images and 162 am-pm combined images. Cloud cover percentages were reduced to 6.0%, 6.8% and 5.3%, respectively. And at the same time, the snow cover increased to about 15.2%, 12.2% and 15.1%, respectively, which tend to be best representation of snow cover.

Figure 3 is a sample image of MOD10A1 product for the date December 4th, 2003. In the image, high cloud coverage, which is in green color, is displayed. Figure 4 is a sample image of MYD10A1 product of afternoon image for the same date. Comparing with the morning image, there seems less cloud coverage. Some area has cloud in the morning, however, the cloud clears in the afternoon. After combining these two images, an am- pm composite image can be generated. Further combination of several days' images using the algorism we mentioned previously, a multi-day am-pm composite image is created. Figure 5 is the sample image of the MODMYD10MC product of the combination of two days (Dec 4th , and Dec 3rd, 2003). As can be seen from this image, snow coverage has been increased, while cloud coverage has been decreased. Thus, the composite product has removed the disturbance of cloud contamination efficiently, which provide us with a more representative image of snow cover extent.

Trend of Snow Cover Change between 2000 and 2007

Based on the results of validation and mean snow and cloud cover comparison, the following mean snow cover change chart is generated under the results of multi-day am-pm images from 2002-2007. 2000 and 2001 are years which have only am images. The results were got from the multi-day am images.

Figure 2 displays the trend of the snow cover change of the Upper Rio Grande Basin during the period of 2000 to 2007. The snow area extent dropped slightly in 2000 to 2002, and then had a sharp increase in the period of 2002 to 2003, from 6.2% to 24.9%. Unexpectedly, it started to decrease in 2003 and then increase in 2004. Apparently, the mean snow cover in the year 2005-2006 has the largest decrease from over 30% to approximately 10%. The lowest mean snow cover happened in the period of 2001-2002 (6.2%), and the highest mean snow cover was in the period of 2004-2005. And we can foresee the increase of snow cover in the year 2007. Overall, there is no fixed trend of increase or decrease of mean snow cover through the year 2000 to 2007. Though global warming is becoming an undisputable fact, the response of snow cover on this issue is not as expected as it should be. The trend of the snow cover change showed a fluctuation in the seven study years.

5. CONCLUSION

Among the 8 MODIS standard and generated products, the multi-day am-pm composite product is believed to be the best representative one in mapping snow area extent. Comparing to the daily products, which has relatively high cloud coverage, the new

products alleviated the contamination of cloud blockage by reducing the cloud cover to less than 10%. Besides, the composite product generated more cloud-free images (162) than 8-day products (47), and had a better temporal resolution. However, the overall validation accuracy of MODIS products is not as good as the one did in Xinjiang area. (Wang, in press). The difference of these to studies is the ground data used for comparison. Instead of using typical snow depth for comparison with MODIS data, the Snow Water Equivalent (SWE) is used, which has limitation especially during rainfall season, since the SWE might be contaminated by rainfall. The cryosphere integrates climate variations over a wide range of time scales, making it a natural sensor of climate variability and providing a visible expression of climate change. (IPCC, 2007). Snow cover change trend derived by the MODIS composite product displayed a fluctuated curve. Climate change associated with increased greenhouse gas emissions may indeed affect future snow cover extent over North America. However, the response to greenhouse gas forcing may be nonlinear.

Reference

Dorothy K. Hall, G. A. R. (2007) Accuracy assessment of the MODIS snow products. *Hydrological Processes* **21**(12): 1534-1547.

Hall, D. K., Riggs, G. A., Salomonson, V. V., DiGirolamo, N. E. & Bayr, K. J. (2002) MODIS snow-cover products. *Remote Sensing of Environment* **83**(1-2): 181-194.

Tekeli, A. E., Akyurek, Z., Arda Sorman, A., Sensoy, A. & Unal Sorman, A. (2005) Using MODIS snow cover maps in modeling snowmelt runoff process in the eastern part of Turkey. *Remote Sensing of Environment* **97**(2): 216-230.

Zhou, X., Xie, H. & Hendrickx, J. M. H. (2005) Statistical evaluation of remotely sensed snow-cover products with constraints from streamflow and SNOTEL measurements. *Remote Sensing of Environment* **94**(2): 214-231.

Klein, A. G. & Barnett, A. C. (2003) Validation of daily MODIS snow cover maps of the Upper Rio Grande River Basin for the 2000-2001 snow year. *Remote Sensing of Environment* **86**(2): 162-176.

Bella, A., Duckstein, L. & Szidarovszky, F. (1996) A multicriterion analysis of the water allocation conflict in the Upper Rio Grande basin. *Applied Mathematics and Computation* **77**(2-3): 245-265.

Costigan, K. R., Bossert, J. E. & Langley, D. L. (2000) Atmospheric/hydrologic models for the Rio Grande Basin: simulations of precipitation variability. *Global and Planetary Change* **25**(1-2): 83-110.

Songweon Lee, A. G. K. T. M. O. (2005) A comparison of MODIS and NOHRSC snow-cover products for simulating streamflow using the Snowmelt Runoff Model. *Hydrological Processes* **19**(15): 2951-2972.

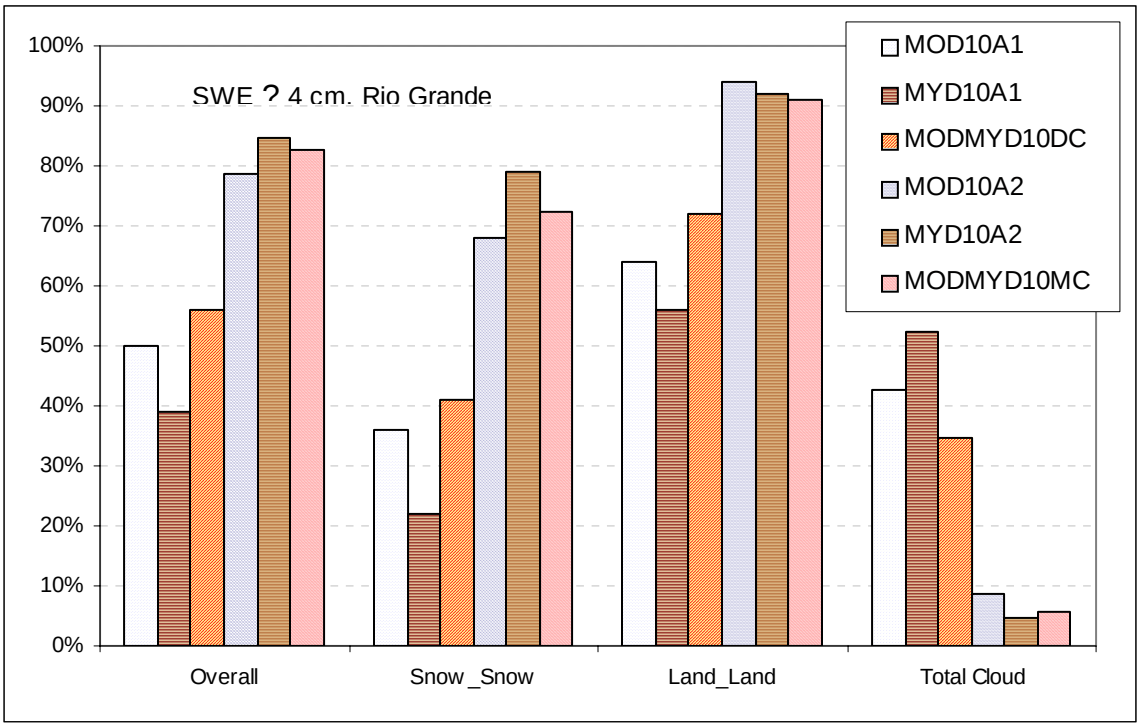

Figure 1 Comparison accuracies of 6 MODIS Snow cover products in terms of overall classification, cloud to cloud, snow to snow, and land to land.

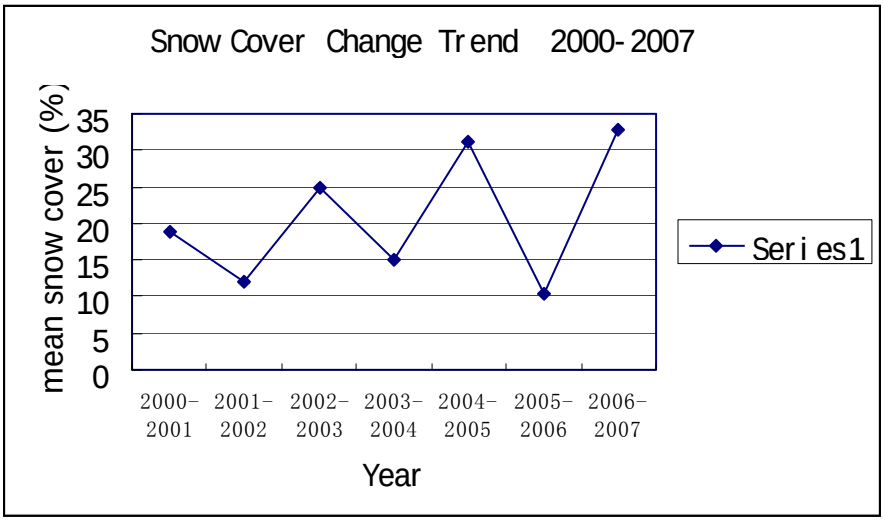

Figure 2 Time series of snow cover change from 2000 to 2007 generated based on the MODIS MODMYD10MC product

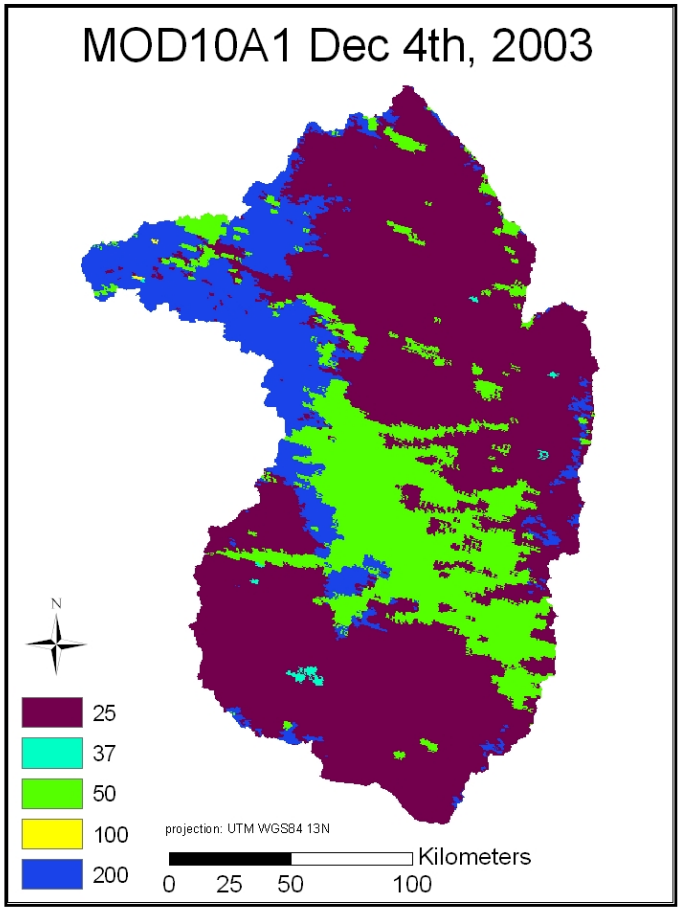

1

2 Figure 3 Map of MOD10A1 image of December 4th , 2003, showing the snow, cloud and

3 land coverage in the morning of the day.

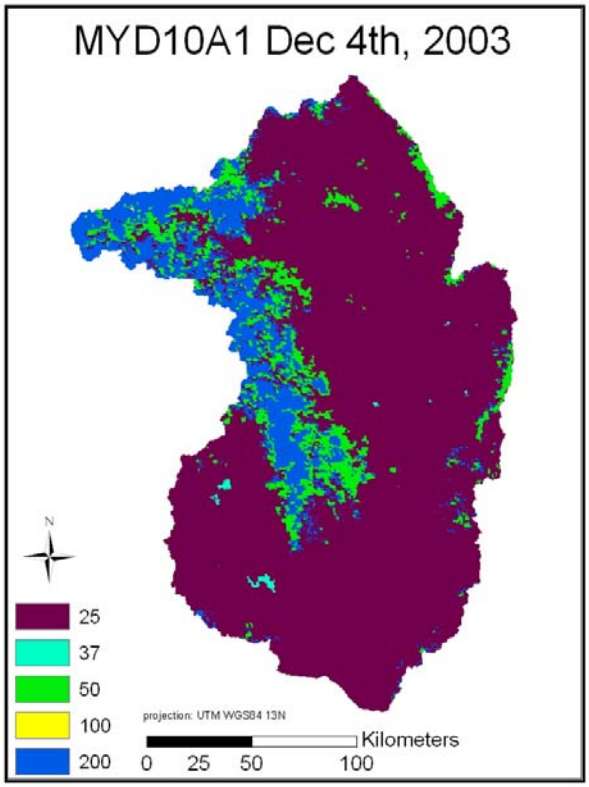

1

2 Figure 4 Map of MYD10A1 image of December 4th , 2003, showing the snow, cloud and

3 land coverage in the afternoon of the day

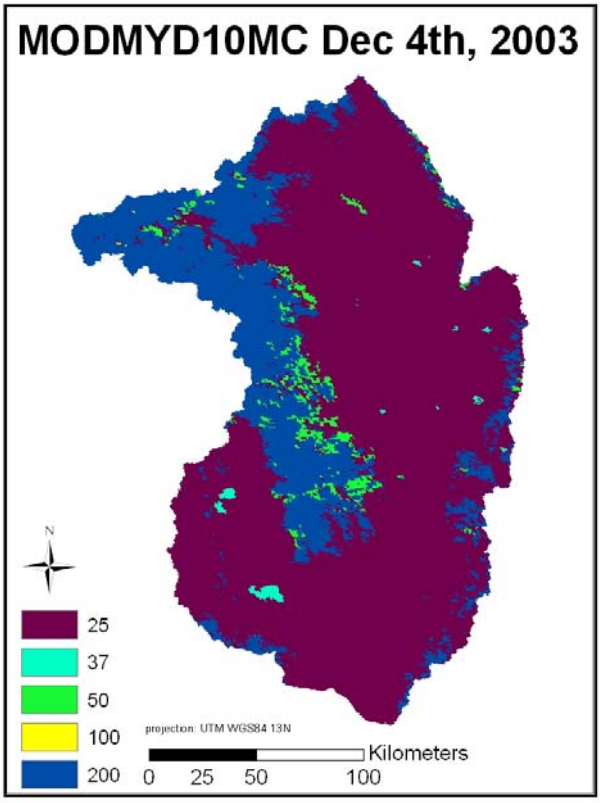

Figure 4 Map of MODMYD10MC image of December 3rd and 4th, 2003. It is the multi-day composite image of am-pm, showing snow, cloud and land coverage.

Table 1. Error matrix between MOD10A1 and ground measurements in the 2003-04 hydorlogic year at 15 stations on Rio Grande Basin, USA

Ground observations	Total	MOD10A1			Accuracy after cloud removed*
	5325	Snow	Land	Cloud	
Land (SWE < 1 cm)	2699	40	1737	922	98%
	51%	1%	64%	34%	
Fractional Snow (SWE =1 - 4 cm)	284	86	72	126	54%
	5%	30%	25%	44%	
Snow (SWE >= 4 cm)	2342	832	292	1218	74%
	44%	36%	12%	52%	

Table 2. Error matrix between MYD10A1 and ground measurements in the 2003-04 hydorlogic year at 15 stations on Rio Grande Basin, USA

Ground observations	Total	MYD10A1			Accuracy after cloud removed*
	5325	Snow	Land	Cloud	
Land (SWE < 1 cm)	2699	23	1522	1154	0%
	51%	1%	56%	43%	
Fractional Snow (SWE =1 - 4 cm)	284	40	83	161	33%
	5%	14%	29%	57%	
Snow (SWE >= 4 cm)	2342	515	354	1473	59%
	44%	22%	15%	63%	

1

Table 3. Error matrix between MOD10A2 and ground measurements in the 2003-04 hydorlogic year at 15 stations on Rio Grande Basin, USA

Ground observations	Total	MOD10A2			Accuracy after cloud removed*
	690	Snow	Land	Cloud	
Land (SWE < 1 cm)	328	9	307	12	97%
	48%	3%	94%	4%	
Fractional Snow (SWE =1 - 4 cm)	26	8	16	2	33%
	4%	31%	62%	8%	
Snow (SWE >= 4 cm)	336	228	62	46	79%
	49%	68%	18%	14%	

2

Table 4. Error matrix between MYD10A2 and ground measurements in the 2003-04 hydorlogic year at 15 stations on Rio Grande Basin, USA

Ground observations	Total	MYD10A2			Accuracy after cloud removed*
	690	Snow	Land	Cloud	
Land (SWE < 1 cm)	328	23	303	2	93%
	48%	7%	92%	1%	
Fractional Snow (SWE =1 - 4 cm)	26	15	8	3	65%
	4%	58%	31%	12%	
Snow (SWE >= 4 cm)	336	266	43	27	86%
	49%	79%	13%	8%	

3

Table 5. Error matrix between M0D10MC and ground measurements in the 2003-04 hydorlogic year at 15 stations on Rio Grande Basin, USA

Ground observations	Total	MOD10A1			Accuracy after cloud removed*
	1815	Snow	Land	Cloud	
Land SWE <= 1 cm	1051	29	967	55	97%
	58%	3%	92%	5%	
Fractional Snow SWE=1-4 cm	125	53	62	10	46%
	7%	42%	50%	8%	
Snow SWE>= 4 cm	639	489	106	44	82%
	35%	77%	17%	7%	

1

Table 6. Error matrix between MYD10MC and ground measurements in the 2003-04 hydorlogic year at 15 stations on Rio Grande Basin, USA

Ground observations	Total	MYD10A2			Accuracy after cloud removed*
	714	Snow	Land	Cloud	
Land (SWE < 1 cm)	450	44	83	323	65%
	63%	10%	18%	72%	
Fractional Snow (SWE =1 - 4 cm)	101	16	70	15	19%
	14%	16%	69%	15%	
Snow (SWE >= 4 cm)	163	129	20	14	87%
	23%	79%	12%	9%	

2

Table 7. Error matrix between MODMYD10DC and ground measurements in the 2003-04 hydorlogic year at 15 stations on Rio Grande Basin, USA

Ground observations	Total	MODMYD10DC			Accuracy after cloud removed*
	5325	Snow	Land	Cloud	
Land (SWE < 1 cm)	2699	118	1944	637	94%
	51%	4%	72%	24%	
Fractional Snow (SWE =1 - 4 cm)	284	64	111	109	37%
	5%	23%	39%	38%	
Snow (SWE >= 4 cm)	2342	969	280	1093	78%
	44%	41%	12%	47%	

1

Table 8. Error matrix between MODMYD10MC and ground measurements in the 2003-04 hydorlogic year at 15 stations on Rio Grande Basin, USA

Ground observations	Total	MODMYD10MC			Accuracy after cloud removed*
	2430	Snow	Land	Cloud	
Land (SWE < 1 cm)	1462	68	1330	64	95%
	60%	5%	91%	4%	
Fractional Snow (SWE =1 - 4 cm)	91	40	46	5	47%
	4%	44%	51%	5%	
Snow (SWE >= 4 cm)	877	635	174	68	78%
	36%	72%	20%	8%	

2

Table 9. Error matrix between MODMYD10MC and ground measurements in the 2003-04 winter time at 15 stations on Rio Grande Basin, USA

Ground observations	Total	MODMYD10MC			Accuracy after cloud removed*
	765	Snow	Land	Cloud	
Land (SWE < 1 cm)	18	1	16	1	94%
	2%	6%	89%	6%	
Fractional Snow (SWE =1 - 4 cm)	41	16	24	1	40%
	5%	39%	59%	2%	
Snow (SWE >= 4 cm)	706	546	112	48	83%
	92%	77%	16%	7%	

3

Table10. Comparison of mean cloud and snow cover percentage of different MODIS Terra and Aqua snow cover products during 2003-2004 hydrologic year in Colorado Plateau

	Total images	Mean cloud	Mean snow
MOD10A1	355	39.5%	5.8%

MYD10A1	365	45.1%	3.5%
MODMYD10DC	355	30.6%	6.6%
MOD10A2	47	2.7%	17.1%
MYD10A2	47	4.1%	18.0%
MOD10MC	129	6.0%	15.2%
MYD10MC	111	6.8%	12.2%
MODMYD10MC	162	5.3%	15.1%

1

2

High-resolution imagery provides additional evidence for sea ice dynamics on Mars

Penelope Wagner, Stephen Ackley and Hongjie Xie

Department of Geological Sciences, UTSA,

One UTSA Circle, San Antonio TX 78249-1644

Further examination of additional high-resolution imagery from HRSC and HiRISE have shown features in the Elysium Planitia/Cerebrus Fossae region that resemble sea ice pressure ridges and pile-ups that also have been observed in the Earth's sea ice cover. Ridging features with linear, sinuous, and rectilinear characteristics examined, border darker boundaries that are suggested to be older material. Side-by-side comparisons of Earth and Mars image pairs have indicated highly similar structures in both sets of imagery. From these, we have also made characteristic measurements on for example, the lengths and widths of rafting thrust structures, the "wavelengths" of sinuous ridges, and floe sizes. From these statistics of characteristic structures, we suggest strong similarities in the apparent material behavior on the two planets. Particularly important and more characteristic of sea ice than other materials is that small temperature changes in the material near the melting point (<-5 C) cause large phase changes that result in the highly dynamic transition from ductile to brittle behavior. The ridging comparisons indicate that although the measurements differ, these features require the same two-phase processes of ductile to brittle behavior to form these features. New observations made through HRSC and MARSIS suggest additional evidence of previous sea-ice dynamics inherent in this area. Pedestal craters were observed in the Medusa Fossae region that show many landscape features, such as a concentric pattern of ejecta around the

craters, that suggest water saturated ground. Terrain around some pedestal craters shows fluvial characteristics, such as gully-like features furrowing between two craters. This unique behavior on both planets provides further evidence that sea ice formed on Mars in an earlier epoch.

Introduction

Images found on Mars from the High Resolution Stereo Camera (HRSC) in the Cerebrus Fosse and Elysium Planitia region depicted pile up and ridging features as evidence from early sea ice dynamics on orbit 0032 (Murray et al., 2005). Recent images released for this region include an array of subsequent features that support sea ice processes for the initial observed features. The dark material overlying the lighter material and several pile up features in orbit 32 shows a southwest flow direction as proposed by (Balme, 2006) in the Athabasca valley by observing cleared areas behind and rubble piles in front of some obstructions, such as craters. A footprint taken from orbit 2121 located to the east of the original pile up features show corresponding flows emanating from the northeast as shown with the pile up features. However, channels have been carved out in a southeast direction perpendicular to the initial westward flooding direction. This is exhibited in the southerly pile up and ridging features shown on the bottom of orbit 2121 (Figure 4). Northeast near the Cerebrus Fosse region some pile up features are shown in orbits 2121 and 2110 that show some fluvial activity adjacent and within some craters. Unlike the pile up features previously observed, sediments are widely distributed around the crater. Ripples perceived within the suggested sediment are characteristic of layered sediments in ice

referred to as pedestal craters (Shultz, 2007). Material around general impact craters differ for the reason that impact craters normally form crusted ridges when only consisting of sediment, and there is no consequential event that facilitates surrounding sediment to become displaced as shown in the top of figure 3. Closer observation is illustrated in orbits 2121 and 2110 (Figure 4).

Background

Evidence of sea-ice on Mars near the equator in Elysium Planitia, and Cerebrus Fosse was postulated by Murray et al., 2005, based partially on images showing analogous structures to those reported for Earth's polar regions. Further examination of additional high-resolution imagery from HRSC and HiRISE have shown features that resemble sea ice pressure ridges and pile-up features that have been observed on Earth's sea ice cover. These features were analyzed by conducting measurements on the Mars images, with comparisons of features on Earth. Characteristic measurements on, for example, the lengths and widths of rafting thrust structures, the "wavelengths" of sinuous ridges, and floe sizes (Figure 1).

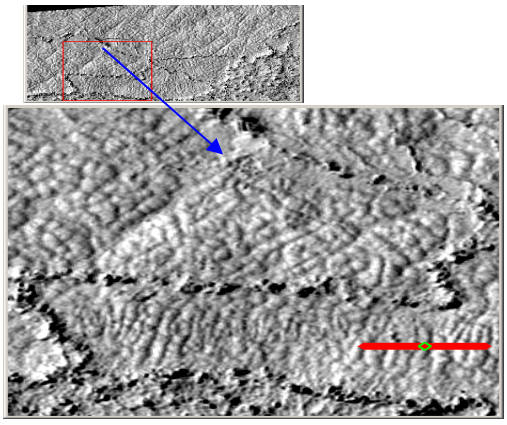

Fig. 1 HiRISE image of Elysium area with ridge-like features at 25cm/pixel (HiRISE).

Mark Hopkins at the Cold Regions Research used a discrete element model to conduct sea-ice ridging comparisons for Earth and Mars. This model generated expected ridging patterns by setting the parameters for each planets' elements to simulate the deformation process of sea ice. Some pile-up features near the Cerebrus Fosse location on Mars were measured to compare the ratio of cleared area, created by the pile-ups, with the features themselves (Figure 2).

Figure 2. Pile up features indicated by the arrows showing cleared areas behind the crater at 10m per pixel (HRSC).

There was a direct correlation between the two planets to infer that the higher amplitudes of the sinusoidal ridging features and pile-up heights of craters in Mars are related to the differences in potential energy and normal forces associated with each environment (Ackley et al., 2006). Particularly important and more characteristic of sea ice than other materials is that small temperature changes in the material near the melting point (<5°C) cause large phase changes that result in a highly dynamic transition from ductile to brittle behavior. From these statistics of characteristic structures, there seems to be a strong similarity in the apparent material behavior on the two planets that is indicative of sea ice.

Inferences from the large-scale behavior are also interpretable in terms of characteristic material properties, giving potentially fuller information in future on the micro structural composition of the ice cover on Mars and its thermodynamic evolution.

Features of Pedestal Craters

Through the process of mapping pile-up features using ArcGIS, the goal was to establish some direction vectors based on the flow features attributed to the cleared areas behind the pile-ups. However, further craters have been discovered in the Elysium Planitia and Medusa Fosse region that could be attributed to any underlying sea ice dynamics. These are pedestal craters that are normally found in the higher latitudes near the poles, particularly in the north (Barlow, 2005). Unlike the previous craters with pile-ups that have a 1:2 ratio to their following cleared areas, pedestal craters are characterized by their evenly distributed ejecta that has been elevated, and concentrically formed around the crater. Early attempts were controversial in that this phenomena relied primarily on an Aeolian deflation erosion model from fine-grained sand, ash, or debris accumulated from air fall deposits (Shultz, 2007, and Kadish, 2006). This hypothesis suggests subsequent sublimation, and deflation of fine-grained material that eventually leaves the ejecta material balanced above the crater. However, pedestal craters formed from sea ice mechanisms differ from these processes, because not only are the surfaces somewhat uniform, but the ejecta is elevated higher than those shown with dune formations (Figure 3).

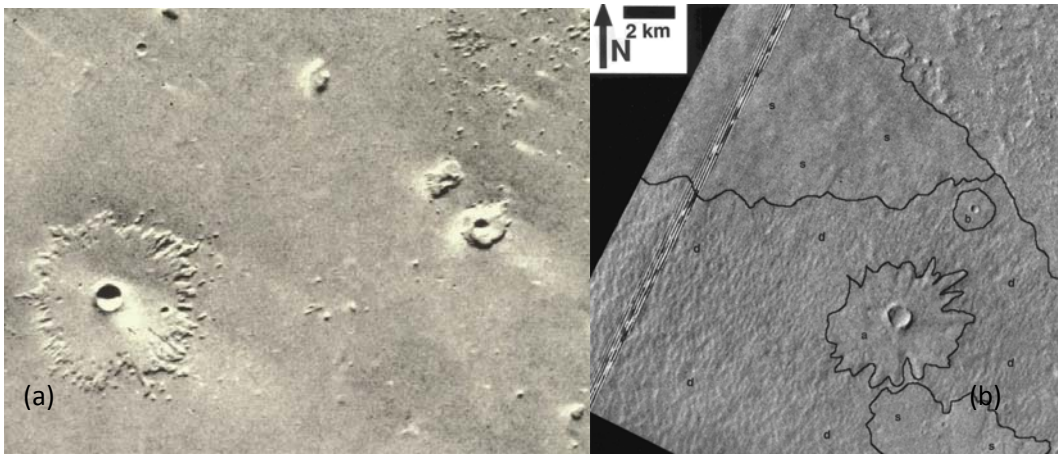

Figure 3. Pedestal craters located in Medusa Fossae(a) at ~50-100 m per pixel (MARSIS). Pedestal craters in the Tharsis region(b) with pedestal craters and ridging attributed to aeolian formations at ~22m/pixel (Viking)(Schultz, 2007 and Edgett, 1997).

Previous studies of pedestal craters in the northern regions were analyzed using the Mars Odyssey Gamma Ray Spectrometer (GRS) to develop a standard ejecta mobility (EM) ratio that measures the ejecta extent with the crater radius, similar to our previous pile-up measurements(Barlow, 2005). The sinuosity was represented b y T=(ejecta perimeter)/(4π(ejecta material). Even though these algorithms suggest pedestal craters in the north are normally smaller and have lower elevation by Barlow, Schultz suggests resolution effects may limit the detection of inner layers of the craters. The circular ejecta patterns on pedestal craters observed in Medusa Fosse were identified using the Mars Advanced Radar for Subsurface and Ionospheric Sounding (MARSIS) instrument on the Mars Express to observe the EM (Schultz, 2007). The correlation of these craters and those found in the northern region that have a high H_2O contents were very similar, because they share similar Double Layer Ejecta (DLE) patterns seen with ejecta material in those regions shown by GRS for the poles. However, craters measured in the 0°N to 60°N latitudes are also showing similar

EM ratio and ejecta mobility as observed by THEMIS VIS and IR imagery (Kadish, 2006). THEMIS images from the Cydonia region suggests that rounded rings of ejecta feature that have a uniform elevation are indicative of a water saturated terrain (Mars Odyssey/THEMIS). Some of the high resolution imagery could be attributed to better resolution on MARSIS or THEMIS instruments, as compared to Viking or other previous instruments used to detect aeolian processes, but additional analysis revealed by the Mars Odyssey Gamma Ray and Neutron Spectrometer (GRNS) also show a strong correlation by comparing these regions with other regions proposed to have been covered in ice during past obliquity cycles.

Images from HRSC (Figure 4)are also showing additional fluvial structures in the areas surrounding the pedestal craters also show signs of fluvial activity with narrow meandering channels that may have formed some adjacent tributary features.

Data

Pedestal craters in the Elysium Planitia/Cerebrus Fossae area southwest of the Medusa Fossae area in figure 4 were mapped out using the ArcGIS program with HRSC footprints at ~10m/pixel to show proposed pedestal craters in this area . This helps to lend additional support to our hypothesis that ridging, pile-up, and crater features were formed from dynamics found in sea ice on Earth.

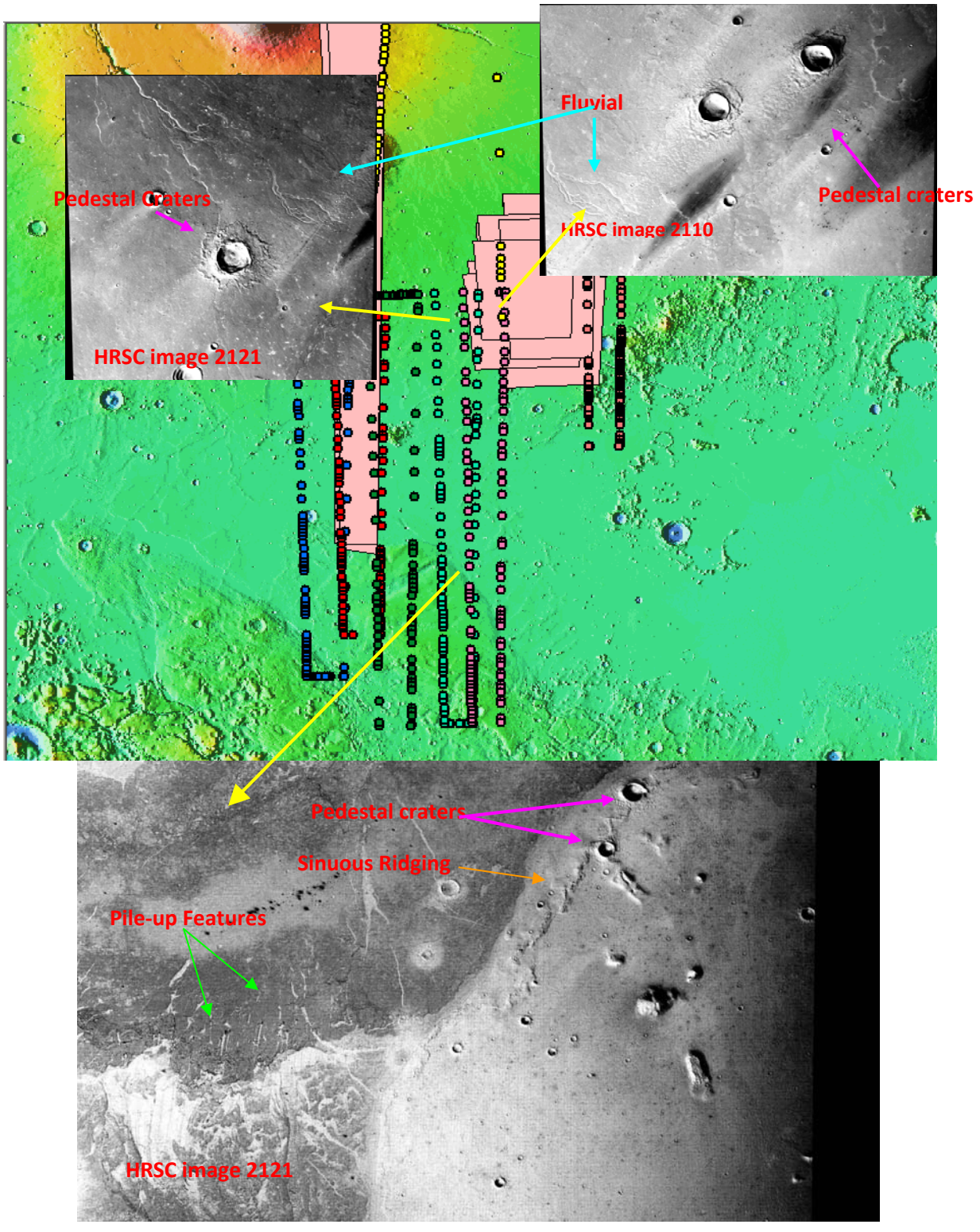

Figure 4. Elysium Planitia/Cerebrus Fossae area mapped using HRSC footprints in ArcGIS to show pedestal crater locations in relation to previous ridging, and pile-up features observed.

Discussion

Pedestal craters located in Medusa Fossae(3a) show more uniform and distinct shadows attributed to higher elevated ejecta material. Surrounding features also show less ridging and yardang features, as compared to that of pedestal craters seen in the Tharsis region (3b). The Viking image has a higher resolution and show distinct dune patterns that appear to be prevalent within the surrounding terrain. However, the MARSIS data is based off of satellite radar signals that can interpolate the surface and subsurface to determine the depth based on the time it takes for the radar beam to pass through the layers and bounce of the plains materials underneath. Visual observation clearly shows little evidence of crusted edges around figure 3a that are normally seen with impact craters and a higher elevation of the surrounding ejecta than 3b. Also, the distribution of linear ridge formations around 3b can indicate more of a prominent Aeolian pattern not picked up by MARSIS. The symmetrical shapes of the ejecta material surrounding the craters in figure 3a and 4 suggest a homogenous sublimation event from ice-rich materials due to weather factors, as opposed to Aeolian processes (Barlow, 2005). Wind direction over the entire 360°area is more or less abnormal , similar to this area, and therefore unable to produce this type of symmetry (Barlow, 2005).

Figure 4 compares similar pedestal craters to that of those detected by MARSIS and helps to correlate ridging and pile-up features already established with ridging model simulations and pile-up features for this area. In addition to the same southwesterly direction as previous pile-up features have shown, the

pedestal craters also appear to have material moving the same course, as seen with the lighter material over the pedestal craters. Also, characteristics of fluvial conditions are seen in between the two pedestal craters in the north of footprints 2110 and 2121. This type of ejecta draping around the crater could have been attributed to a meteorite impact over an ice-rich ground. Therefore, as the climate changes, the mixture of debris and frozen volatiles simultaneously sublime out of the raised ejecta. This leaves the fine-grained sediment to form a concentric circular pattern of layered sediment around the crater rim. These look very similar to other pedestal craters in locations where the evidence for ground ice is supported. Southwest of this area shows additional pile-up features flowing more southward, which is indicated by the lighter material overlying the darker material in the bottom image of figure 4. Although every crater and ridging feature of this area has not been completely mapped out yet, the newly discovered pedestal craters provide additional support to sea ice mechanisms near the equator.

Conclusion

Unless we can accurately compare established pedestal craters formed from Aeolian mechanisms in the Tharsis region to those in the poles where there is definite evidence, we can only hypothesize evidence of sea ice in the Elysium region near the equator. However, by being able to model these conditions and use radar information already obtained offers substantial support that these processes produced analogous structures to those reported for the Earth's polar regions.

References

Balme, M.R., J.B. Murray, S. F. Ackley, J-P Muller, J.R. Kim. (2007), Morphological Evidence For A Sea-Ice Origin For Elysium Planitia Platy Terrain. LPI 38th, 2202

N.G. Barlow, A New Model For Pedestal Crater Formation. LPI 3041(2005)

Kenneth S. Edgett, Icarus 130, 96-114 (1997)

Mark A. Hopkins, JGR 104, No. C6, 13,605-13,613, June 15 1999.

S.J. Kadish et al., Pedestal Crater Distribution and Implications For A New Model of Formation. LPI (2006)

Murray, J.B., Muller, J., Neukum, G., Werner, S., Gasselt, S., Hauber, E., Markiewicz, W., Head, J., Foing, B., Page, D., Mitchell, K., Portyankina, G., (2005) *Evidence from the Mars Express High Resolution Stereo Camera for a frozen sea close to Mars' equator.* Nature vol. 434, pp. 352-355

Peter H. Schultz, Science 318,1080 (2007); published online 5 December 2007(10.1126/science.1151412).